

Relative contributions of sinking and non-sinking carbon to the downward carbon flux

Wei-Lei Wang¹, Frederic Andre Corentin Le Moigne², Robert T. Letscher³, Francois W. Primeau⁴, and Jefferson Keith Moore⁴

¹UC Irvine

²Mediterranean Institute of Oceanography

³University of Hampshire

⁴University of California, Irvine

November 21, 2022

Abstract

The downward flux of organic carbon exported from the surface ocean is of great importance to the Earth's climate because it represents the major pathway for transporting CO from the surface ocean and atmosphere into the deep ocean and sediments where it can be sequestered for a long time. Here we present global-scale estimates for the export fluxes of total, dissolved, and particulate organic carbon (TOC, DOC, and POC, respectively) constrained by observed thorium-234 (Th) activity and dissolved phosphorus (DIP) concentration in a global inverse biogeochemical model for the cycling of phosphorus and Th. We find that POC export flux is low in the subtropical oceans, indicating that a projected expansion of the subtropical gyres due to global warming will weaken the gravitational biological carbon pump. We also find that DOC export flux is low in the tropical oceans, intermediate in the upwelling Antarctic zone and subtropical south Pacific, and high in the subtropical Atlantic, subtropical north Pacific, and productive subantarctic zone (SAZ). The horizontal distribution of DOC export ratio (F/F) increases from tropical to polar regions, possibly due to the detrainment of DOC rich surface water during mixing events into subsurface waters (increasing the strength of the mixed layer pump poleward due to stronger seasonality). Large contribution to the export flux from DOC implies that the efficiency with which photosynthetically fixed carbon is exported as particles may not be as large as currently assumed by widely used global export algorithms.

Relative contributions of sinking and non-sinking carbon to the downward carbon flux

Wei-Lei Wang¹, Frédéric A. C. Le Moigne^{2,3}, Robert Letscher⁴, François W.

Primeau¹, J. Keith Moore¹

Corresponding author: Wei-Lei Wang, Department of Earth System Science, University of California at Irvine, Irvine, California, USA. (weilei.wang@gmail.com)

¹Department of Earth System Science,
University of California at Irvine, Irvine,
CA 92697, USA.

²GEOMAR, Helmholtz Centre for Ocean
Research Kiel, Kiel, Germany.

³Mediterranean Institute of
Oceanography (MIO), UM110, CNRS, IRD,
Aix-Marseille Université, Campus de
Luminy, 13288, Marseille, France

⁴Earth Sciences and Ocean Process
Analysis Laboratory, University of New
Hampshire, Durham, NH 03824, USA

1 **Abstract.** The downward flux of organic carbon exported from the sur-
2 face ocean is of great importance to the Earth's climate because it represents
3 the major pathway for transporting CO₂ from the surface ocean and atmo-
4 sphere into the deep ocean and sediments where it can be sequestered for
5 a long time. Here we present global-scale estimates for the export fluxes of
6 total, dissolved, and particulate organic carbon (TOC, DOC, and POC, re-
7 spectively) constrained by observed thorium-234 (²³⁴Th) activity and dis-
8 solved phosphorus (DIP) concentration in a global inverse biogeochemical
9 model for the cycling of phosphorus and ²³⁴Th. We find that POC export
10 flux is low in the subtropical oceans, indicating that a projected expansion
11 of the subtropical gyres due to global warming will weaken the gravitational
12 biological carbon pump. We also find that DOC export flux is low in the trop-
13 ical oceans, intermediate in the upwelling Antarctic zone and subtropical south
14 Pacific, and high in the subtropical Atlantic, subtropical north Pacific, and
15 productive subantarctic zone (SAZ). The horizontal distribution of DOC ex-
16 port ratio (F_{DOC}/F_{TOC}) increases from tropical to polar regions, possibly
17 due to the detrainment of DOC rich surface water during mixing events into
18 subsurface waters (increasing the strength of the mixed layer pump poleward
19 due to stronger seasonality). Large contribution to the export flux from DOC
20 implies that the efficiency with which photosynthetically fixed carbon is ex-
21 ported as particles may not be as large as currently assumed by widely used
22 global export algorithms.

1. Introduction

23 The biological pump transfers a large amount of photosynthetically produced organic
24 carbon from the surface ocean into subsurface waters that are isolated from the atmosphere
25 [*Archer et al.*, 2000; *Eppley and Peterson*, 1979] a process that regulates atmospheric CO₂,
26 and thus influences the Earth's climate [*Kwon et al.*, 2009]. Because particulate organic
27 carbon (POC) has a fast sinking speed it is thought to be a key control on the strength of
28 the biological carbon pump [e.g. *Allredge et al.*, 1993; *Giering et al.*, 2014]. Consequently
29 empirical relationships have been devised to relate temperature and satellite-based esti-
30 mates of net primary production (NPP) to the ef-ratio, which is defined as the ratio of
31 export production or new production to total primary production [*Dunne et al.*, 2005;
32 *Henson et al.*, 2011; *Laws et al.*, 2011; *Guidi et al.*, 2015]. These empirical algorithms
33 commonly assume that the ef-ratio is positively correlated to NPP and negatively corre-
34 lated to sea surface temperature (SST). However, export fluxes estimated from different
35 versions of these simple algorithms can vary by a factor of three (4 - 12 Pg C yr⁻¹), though
36 part of the difference may be caused by the choice of export depth as well methodological
37 and data coverage issues [*Henson et al.*, 2011]. Furthermore, these algorithms have been
38 challenged by direct observations [e.g. *Lam and Bishop*, 2007; *Henson et al.*, 2012; *Maiti*
39 *et al.*, 2013; *Cavan et al.*, 2015; *Laurenceau-Cornec et al.*, 2015; *Le Moigne et al.*, 2016]
40 showing that in highly productive upwelling regions such as the Southern Ocean (high
41 productivity low export ratio region) NPP is negatively correlated to the ef-ratio [*Maiti*
42 *et al.*, 2013; *Laurenceau-Cornec et al.*, 2015]. Biome-specific fittings have therefore been
43 developed to better predict export efficiency from NPP and SST [*Britten and Primeau*,

44 2016]. However, the biome-specific models based on different but plausible functional
45 forms predict large differences ($> 100\%$) that cannot be ruled out because of limited
46 observation of POC export fluxes, especially in the Indian Ocean and Subtropical gyres
47 [*Britten and Primeau, 2016*].

48 The importance of non-gravitational export pathways, such as those caused by phys-
49 ical subduction and/or zooplankton migration, are often ignored but *Boyd et al.* [2019]
50 suggest that non-gravitational export pathways that acts on both sinking and suspended
51 particles can account for as much carbon export as from the gravitational carbon pump.
52 *Emerson* [2014] analyzed annual net community production (ANCP), which is equal to
53 the export flux of organic matter over an annual cycle, at three time series sites (Hawaii
54 Ocean Time-series (HOT), Bermuda Atlantic Time-series Study (BATS), and ocean Sta-
55 tion Papa (OSP)). He concluded that POC export flux is 3-4 times lower than the mass
56 balance estimates of ANCP, indicating the dominant roles played by non-sinking particle
57 export, DOC export, and/or zooplankton migration. *Hansell et al.* [2009] estimated that
58 DOC export contributes $\sim 20\%$ of the biogenic carbon export from the surface ocean.
59 *Letscher et al.* [2015] estimated a global DOC export flux of $2.28 \text{ Pg C yr}^{-1}$ using the
60 Biogeochemical Elemental Cycling (BEC) model with dissolved organic matter (DOM)
61 cycling parameters optimized to best match a global compilation of DOM observations.
62 *Roshan and DeVries* [2017] estimated a similar climatological DOC export flux by cou-
63 pling a neural network extrapolated DOC field with an ocean circulation model. They
64 suggested that the DOC export flux is highest in the subtropical gyres implying that the
65 role of DOC in the biological pump will be enhanced in the future because the subtropical
66 gyres are predicted to expand with global warming. A potential caveat pointed out by

67 *Roshan and DeVries* [2017] is that the DOC observations were mostly collected during
68 the summer season in regions with relatively low NPP. The goodness of fit of their annual-
69 averaged model to summer field data ($R^2 = 0.95$ overall) does not rule out the potential
70 importance of seasonality, especially in the high-latitude oceans. In summary, DOC and
71 non-sinking particle exports contribute a significant fraction of the total organic carbon
72 export but the magnitude of this contribution remains uncertain as indicated by the in-
73 consistency of the previous estimates. This motivates us to revisit the relative importance
74 of the non-gravitational pathway.

75 Biogeochemical inverse models can in principle be used to estimate global scale carbon
76 export. For example, *Teng et al.* [2014] used a coupled inverse model for phosphorus and
77 carbon cycles constrained by DIC and DIP observations, and estimated regionally-varying
78 C:P ratios, from which they estimated a global-scale total carbon export of 9.13 Pg C
79 yr^{-1} . Using a similar approach, but for a model of the marine nitrogen and phosphorus
80 cycles with a constant C:N ratio, *Wang et al.* [2019a] estimated a global carbon export of
81 ~ 12 Pg C yr^{-1} . However, both models are unable to accurately separate the contribution
82 of sinking POC export from the total export. This is in part due to the fact that *Teng*
83 *et al.* [2014] did not include organic matter constraint in their model. Whereas, *Wang*
84 *et al.* [2019a] did use observed DON as a constraint but its weight in the objective function
85 was small compared to those of DIP and DIN. More importantly, it is not clear from these
86 studies if and how the C:P ratios might be different for DOC compared to POC. Here we
87 use ^{234}Th observations to further constrain the relative contributions of DOC and POC
88 to the total export.

²³⁴Th has been widely used to estimate regional ocean POC export [*Black et al.*, 2018; *Buesseler et al.*, 1995]. Its successful application is due to its strong particle affinity and short decay half-life of 24.1 days, which make it an excellent tracer for surface ocean processes. In addition, its radioactive parent, ²³⁸U, is a conservative tracer and almost uniformly distributed in the ocean, which offers ²³⁴Th a constant source in the water column. *Henson et al.* [2011] made the first attempt to estimate global carbon export using ²³⁴Th method. They constrained a thorium based export ratio (“ThE-ratio”) using in-situ estimates of ²³⁴Th-based export and satellite-derived SST and PP, and obtained a low POC export rate of 4 Pg C yr⁻¹. They then assumed that DOC export flux was 20% of total carbon export rate, and concluded that the globally integrated carbon export was 5 Pg C yr⁻¹, which on average is lower than previous inverse model and satellite-based estimates [e.g. *Laws et al.*, 2011; *Guidi et al.*, 2015; *Teng et al.*, 2014; *Wang et al.*, 2019a]. The inconsistency between ²³⁴Th-based and satellite-based estimates provides a further motivation for our study.

Here we use a data-constrained ocean circulation model [*DeVries and Primeau*, 2011; *Primeau et al.*, 2013] coupled with a phosphorus (P) cycling model to extrapolate sparse ²³⁴Th activity measurements (Table A1) to the global ocean and then use an estimate of the POC: ²³⁴Th ratio to evaluate the global export of POC as well as its regional variations. The extrapolation of the ²³⁴Th activity measurements is performed by optimizing a set of biogeochemical parameters (Methods, Fig. A1, and Table A2) to best match the database of ²³⁴Th activity measurements. TOC export flux is diagnosed from the phosphorus model using previously estimated spatially-varying C:P ratios. We then obtain the DOC export flux from propagating the difference between the TOC and POC export fluxes in a Monte

112 Carlo run (See Methods and Fig. 1). This allows us to assess the relative importance
113 of DOC export in high productivity low export regimes. We discuss the implications of
114 DOC export flux for the efficiency of biological pump. Furthermore, because the model
115 produces separate estimates for the contribution from the dissolved and particulate phases
116 of both C and P, we are able to obtain separate global-scale estimates for the C:P ratio
117 of non-sinking organic matter and sinking organic matter.

2. Methods

118 In a steady-state ocean with no sinking particles, ^{234}Th and its parent ^{238}U are expected
119 to be in a secular equilibrium with the activity of ^{234}Th equal to that of ^{238}U . In the ocean,
120 its insolubility and strong particle affinity enable thorium to easily become attached to
121 sinking particles and be carried out of the surface ocean in a process known as particle
122 scavenging. If the scavenging removal process is fast enough, it will cause a deficit in
123 ^{234}Th activity relative to the ^{238}U activity. Since the abundance of particles decreases
124 with depth, the scavenging strength also decreases with depth allowing ^{234}Th to reach
125 secular equilibrium at depth.

126 By measuring ^{234}Th distribution at different depths and integrating its deficit relative
127 to ^{238}U , and assuming a POC: ^{234}Th ratio one can estimate POC flux [*Buesseler et al.*,
128 1992]. This approach has been applied under both steady and non-steady state [*Cochran*
129 *et al.*, 2000; *Savoie et al.*, 2006; *Buesseler et al.*, 2009; *Cai et al.*, 2010].

2.1. Phosphorus model

130 We model phosphorous cycling by tracing its three phases, dissolved inorganic phospho-
131 rus [DIP], non-sinking organic phosphorus [DOP], and sinking particulate organic phos-

132 phorus [POP]. We use square brackets to denote concentration/activity. The governing
 133 equations for phosphorus cycle are as follow,

$$\begin{aligned}
 \left[\frac{d}{dt} + \mathbf{T} \right] [\text{DIP}] &= -\gamma[\text{DIP}] + \kappa_d[\text{DOP}] + \kappa_g([\text{DIP}] - \overline{[\text{DIP}]}_{\text{obs}}), \\
 \left[\frac{d}{dt} + \mathbf{T} \right] [\text{DOP}] &= \sigma\gamma[\text{DIP}] + \kappa_p[\text{POP}] - \kappa_d[\text{DOP}], \\
 \left[\frac{d}{dt} + \mathbf{S} \right] [\text{POP}] &= (1 - \sigma)\gamma[\text{DIP}] - \kappa_p[\text{POP}],
 \end{aligned} \tag{1}$$

where κ_d is DOP respiration rate constants, and is optimized in the inversion. κ_p (30 day)⁻¹ is the particle dissolution rate constant. κ_g (10⁶ yr)⁻¹ is a weak restoring rate coefficient used to set the mean phosphate concentration to $\overline{[\text{DIP}]} = 2.17$ mmol/m⁻³, the observed volume weighted mean DIP concentration. σ is a production partition parameter that determines how much new production is allocated to DOP and POP. γ is DIP uptake rate, which is modeled using satellite derived NPP and two adjustable parameters (α and β) as follows,

$$\gamma(\mathbf{r}) \equiv \begin{cases} \alpha \frac{\left[\frac{1}{r_{\text{C:P}}} \frac{\text{NPP}(\mathbf{r})}{\text{NPP}_0} \right]^\beta}{\frac{[\text{DIP}]_{\text{obs}}(\mathbf{r})}{[\text{DIP}]_0}}, & \text{if } z < z_c, \\ 0, & \text{otherwise,} \end{cases} \tag{2}$$

134

135 where $r_{\text{C:P}}$ is carbon to phosphorus ratio, NPP_0 and $[\text{DIP}]_0$ are set to 1 mmol C m⁻² s⁻¹
 136 and 1 mmol m⁻³, respectively, and are used to ensure α has dimensions of inverse time.
 137 z_c is euphotic zone depth, in the model, it is the depth of the first two layers (~ 73 m)
 138 [*Teng et al.*, 2014].

139 Non-sinking phosphate (DIP and DOP) are transported by advection and diffusion that
 140 are modeled using an advection-diffusion transport operator, \mathbf{T} , defined so that $\mathbf{T}[C] \equiv$
 141 $\nabla \cdot (\vec{U}[C] - \mathbf{K}\nabla[C])$. This operator was optimized using multiple tracers, including

142 salinity, temperature, sea surface height, CFC11, pre-bomb radiocarbon, and phosphate
 143 [*DeVries and Primeau, 2011; Primeau et al., 2013*]. The vertical transport of sinking
 144 particulate organic phosphorus is modeled using a particle flux divergence operator, \mathbf{S} ,
 145 that is built based on the power law attenuation function known as Martin curve [*Fu and*
 146 *Primeau, 2017*]. The Martin curve exponential b values are optimized in inversion (Fig.
 147 A1).

2.2. Thorium model

148 We model thorium cycling by tracing its two phases, a “dissolved” phase ($[\text{Th}_d]$)
 149 that is not associated with particles and a “particulate” phase ($[\text{Th}_p]$) that is ad-
 150 sorbed on sinking particles. Dissolved ^{234}Th is produced by its conservative parent
 151 ($[\text{}^{238}\text{U}] \left(\frac{\text{dpm}}{\text{m}^{-3}}\right) = 78.6\text{S} - 315$, where S is salinity) via alpha decay [*Owens et al., 2011*], and
 152 lost by its own alpha decay. It is also lost by adsorption onto particles, which is modeled
 153 as a product of $[\text{POP}]$ and $[\text{Th}_d]$ with an adjustable adsorption rate constant κ_1 (Eq. 3).
 154 Particulate thorium is returned back to the dissolved phase via particle dissolution and
 155 desorption, and also sinks in the water column.

The governing equations for thorium cycling are the following,

$$\begin{aligned} \left[\frac{d}{dt} + \mathbf{T}\right][\text{Th}_d] &= \lambda_{234}([\text{}^{238}\text{U}] - [\text{Th}_d]) + (\kappa_p + \kappa_{-1})[\text{Th}_p] - \kappa_1[\text{POP}][\text{Th}_d], \\ \left[\frac{d}{dt} + \mathbf{S}\right][\text{Th}_p] &= -(\lambda_{234} + \kappa_p + \kappa_{-1})[\text{Th}_p] + \kappa_1[\text{POP}][\text{Th}_d], \end{aligned} \quad (3)$$

156 where λ_{234} is the decay constant for ^{234}Th , $[\text{}^{238}\text{U}]$ is uranium-238 activity in dpm m^{-3} , κ_1
 157 and κ_{-1} are adsorption and desorption rate constants, respectively, which are optimized
 158 in the inversion.

159 Sinking of particulate ^{234}Th is modeled using the same flux divergence operator \mathbf{S} as
 160 in the phosphorus model. Transport of dissolved ^{234}Th is modeled using advection and
 161 diffusion transport operator (\mathbf{T}).

2.3. Parameter optimization and error estimations

Parameter optimization is conducted using Bayesian inversion method [*Teng et al.*, 2014; *Wang et al.*, 2019a, b]. The observed DIP concentration and ^{234}Th activity are used to constrain the model. We obtain phosphorus (P) and thorium (Th) fields by solving the governing equations for P and Th (Eqs.1-3). The governing equations for P-cycle model are linear, and thus can be solved using direct matrix inversion. With POP concentration from the P model, the Th equations are also linear, and are therefore solved by direct matrix inversion. We minimize the difference between model outputs and observations by optimizing a set of parameters controlling P and Th cycle using the following objective function.

$$f = e_{\text{P}}' \frac{1}{\mathbf{W}_{\text{P}}} e_{\text{P}} + e_{\text{Th}}' \frac{1}{\mathbf{W}_{\text{Th}}} e_{\text{Th}},$$

where $e_{\text{Th}} = [\text{Th}_{\text{mod}}] - [\text{Th}_{\text{obs}}]$ and $e_{\text{P}} = [\text{DIP}_{\text{mod}}] - [\text{DIP}_{\text{obs}}]$. \mathbf{W}_{Th} and \mathbf{W}_{P} are precision matrices for ^{234}Th and DIP. \mathbf{W}_{Th} is defined using the following equation,

$$\mathbf{W}_{\text{Th}} = \frac{1}{\sigma_{\text{Th}}^2} \mathbf{V},$$

where \mathbf{V} is grid-box fractional volumes ($\mathbf{V} = \text{diag}(\Delta V_i / \sum_i \Delta V_i)$), and σ_{Th} is defined,

$$\sigma_{\text{Th}}^2 = ([\text{Th}_{\text{mod}}]) - \mu_{\text{Th}})' \mathbf{V} (([\text{Th}_{\text{mod}}] - \mu_{\text{Th}})$$

with

$$\mu_{\text{Th}} = \frac{\Sigma([\text{Th}_{\text{obs}}] \mathbf{V}_{\text{Th}})}{\Sigma \mathbf{V}_{\text{Th}}},$$

162 where \mathbf{V}_{Th} is grid box volume, and the subscript Th represents the grid boxes with ^{234}Th
 163 observations. The DIP weighing matrix \mathbf{W}_{P} is defined similarly.

164 The optimization is conducted using Matlab's `fminunc` function, which is efficient be-
 165 cause we are able to supply the first and second derivatives of the objective function. The
 166 optimization generally finishes within 100 iterations. The optimal model parameters are
 167 presented in Table A2 and Fig. A1. Parameter errorbars that correspond to ± 1 stan-
 168 dard deviation, are calculated according to the method described in *Wang et al.* [2019a].
 169 We optimized a total of 17 model parameters to minimize the difference between model
 170 output and observations.

2.4. Calculation of carbon flux

The POC flux (F_{POC}) is calculated by integrating the deficit between $[^{238}\text{U}]$ and $[^{234}\text{Th}]$
 over the studied depth and multiplying by a POC to ^{234}Th ratio (Eq. 4). Here we use a
 globally constant integration depth ($z_0=114$ m, depth of the upper three model layers),
 which is close to the suggested integration depth [*Buesseler et al.*, 2006].

$$F_{\text{POC}} = R_{\text{POC}:^{234}\text{Th}} \times \lambda \int_0^{z_0} ([^{238}\text{U}] - [^{234}\text{Th}]) dz. \quad (4)$$

171 The ratio of POC to ^{234}Th is calculated using the following empirical equation
 172 ($R_{\text{POC}:^{234}\text{Th}} = 135.3 \times z^{-0.795}$) [*Owens et al.*, 2015]. Previous studies indicate that this
 173 ratio may have large seasonal, geographical, and depth variations, and can also vary sig-
 174 nificantly based on sampling methods [*Buesseler*, 1998]. However, by compiling data
 175 covering large geographical regions and different seasons, *Owens et al.* [2015] suggested
 176 that the variability of $R_{\text{POC}:^{234}\text{Th}}$ decreases dramatically as depth increases, and becomes
 177 almost constant at depth of ~ 100 m. In the present study, we apply the empirical relation-

178 ship at our studied depth of 114 m, and consider its possible variations in the uncertainty
 179 analysis (See next section). Thus, we are hypothesizing that a constant $R_{\text{POC}:^{234}\text{Th}}$ ratio
 180 produces an accurate carbon export estimate.

181 The POC flux below the first three layers is calculated based on the following power
 182 law function ($F_{\text{POC}}(z) = F_{\text{POC}}(z_0) (z/z_0)^{-b}$) [*Martin et al.*, 1987], where z_0 is the refer-
 183 ence depth (114 m), z is the depth where POC flux is calculated, and b is Martin curve
 184 exponentials that are optimized in the model (Fig. A1).

185 Total carbon export is diagnosed from the phosphorus model (See Fig. 1), which is
 186 constrained using both phosphate concentration and ^{234}Th activity. We first calculate
 187 total organic phosphorus (TOP) export based on an adjoint method [*Primeau et al.*,
 188 2013], which tracks the export and subsequent remineralization of DOP and POP. Only
 189 DOP and POP respired/dissolved below the studied depth is counted as export. We
 190 then convert total phosphorous (DOP+POP) export to total carbon export by imposing
 191 spatially variable C:P ratios. To make this ratio more robust, we averaged the estimated
 192 C:P ratios from *Teng et al.* [2014] and *Wang et al.* [2019a] (Table 1).

2.5. Uncertainty analysis

193 The uncertainty analysis is conducted using a Monte Carlo method. Errors from three
 194 major sources are considered: 1) Model parameters and their associated error bars, 2)
 195 C:P ratio that is used to convert total phosphorus export to carbon export, and 3) POC
 196 to ^{234}Th ratio. Parameters are drawn randomly from a normal distribution with mean
 197 defined by optimal model parameters and variance defined by the covariance matrix. The
 198 C:P ratio from *Teng et al.* [2014] is selected randomly using the regional errorbars quoted
 199 in their paper. The POC to ^{234}Th ratio is drawn from a normal distribution with a mean

200 defined by $\text{POC:Th} = 135.3z^{-0.795}$ at $z = 114$ m and a variance of 0.25, which creates a
201 range between ~ 2.3 to ~ 4.0 that is consistent to Fig. 8 of Ref.[*Owens et al.*, 2015]. In the
202 Monte Carlo analysis, we recalculate TOC and POC export fluxes based on parameters
203 from each random drawn. DOC export flux is calculated as the difference between TOC
204 and POC export fluxes at each iteration. We report median values and 95% confidence
205 intervals that are based on a sample size of 1000.

3. Results and discussion

3.1. Global distribution of ^{234}Th

206 Overall, our model shows a reasonably good agreement with available ^{234}Th activity
207 measurements ($R^2 = 0.46$, Fig. A2b), the other 54% of variance can partially be explained
208 by seasonal variability. Spatially, our model results correlate well with observations (Fig.
209 2), ^{234}Th activity (which is inversely proportional to the export flux of particles) is gen-
210 erally high in subtropical gyres, low to intermediate in the Southern Ocean and high in
211 productive coastal regions. From the first (0-36 m) to third layer (73-114 m), ^{234}Th ac-
212 tivity increases, indicating that scavenging strength becomes weaker, and ^{234}Th and ^{238}U
213 are approaching secular equilibrium (See also Fig. A3).

3.2. Particulate Carbon export fluxes

214 Globally integrated, we estimate a POC export flux rate of 4.81 (95% CI 4.00-5.52) Pg
215 C yr^{-1} (Fig. 3) at the bottom of the third grid box (114 m). If we scale up the export flux
216 to 100 m using Martin curve function and the optimal b values (Fig. A1), our estimate
217 becomes to 5.28 (95% CI 4.39-6.06) Pg C yr^{-1} . While our globally integrated POC export
218 flux estimate disagrees with previous estimates taken individually, it is consistent with

219 the ensemble of previous estimates at the same reference depth (100 m). For example,
220 *Harrison et al.* [2018] reported a high global POC export rate of 6.60-6.71 Pg C yr⁻¹
221 whereas *Henson et al.* [2011] obtained a low rate of ~ 4 Pg C yr⁻¹ by scaling up ²³⁴Th
222 based measurements to the whole ocean using a relationship between satellite derived sea
223 surface temperature and POC export observations. *Letscher et al.* [2015] calculated a
224 POC export rate of 6.6 Pg C yr⁻¹ by incorporating optimized DOM recycling parameters
225 into a biogeochemistry model. More importantly, our POC export flux estimates are
226 highly correlated with the in situ measurements [*Mouw et al.*, 2016], which consist mostly
227 of sediment trap data of which only 4% are determined using the ²³⁴Th method (Fig. 4).
228 Geographically, POC flux is high in upwelling and subpolar regions and low in subtropical
229 (Fig. 5a).

3.3. Total Carbon export fluxes

230 Our globally integrated TOC export is 7.74 (95% CI 7.53-7.97) Pg C yr⁻¹ at the depth
231 of 114 m, this number can be scaled up by $\sim 10\%$ to 8.51 Pg C yr⁻¹ at 100 m if we apply
232 the same scaling factor that was used for the POC flux. However, this is a very coarse
233 calculation, because the respiration from DOC is not expected to follow the same Martin
234 curve decay function as used for POC. This estimate of the TOC export flux rate is within
235 the (very wide) range of previous model and satellite based estimates (5-14 Pg C yr⁻¹,
236 Table 1 of *Emerson* [2014]). We compared our regional estimates to those of *Emerson*
237 [2014], who estimated export in four separate biomes: tropical (0-15°), subtropical (15-
238 30°), subtropical/subpolar (30-45°), and subpolar (45-60°). We find that our mean export
239 fluxes for each biome are in agreement (Fig. 6).

240 There are no experimentally determined large-scale annual TOC export flux estimates,
241 because extensive sampling is needed to resolve the seasonal cycle. Thus reliable ANCP
242 estimates are only available at time-series stations. We thus compared our TOC export
243 flux rate with those measured at HOT, BATS, and OSP using mass balance calculations.
244 Our model results (median with 95% CI) have overlapping errorbars with mass balance
245 estimates at HOT ($61.5^{68.8}_{57.9}$ (this study) vs 82.2 ± 23.0 mg C m⁻² day⁻¹), at OSP ($57.9^{65.1}_{54.3}$
246 (this study) vs 75.6 ± 19.7 mol C m⁻² day⁻¹), and at BATS station ($86.8^{94.1}_{75.9}$ (this study)
247 vs 124.9 ± 39.5 mg C m⁻² day⁻¹) [Emerson, 2014], when we scale our TOC export flux to
248 100 m (see above discussion). Our results show that it is critical to report the assumed
249 reference depth explicitly along with the export flux. Based on our optimal b values, a
250 ~ 14 m depth difference (114 m compared to 100 m) can result in a $\sim 10\%$ difference in
251 export flux [Henson *et al.*, 2011]. The export flux difference caused by depth differences
252 can be even larger if we extrapolate to shallower depths due to the negative exponent in
253 the power law model for the flux attenuation.

3.4. Dissolved Carbon export fluxes

254 The DOC definition in our model is slightly different from conventional operationally
255 defined DOC, which is based on filter pore size. In our model, DOC is non-sinking
256 organic matter that can be transported by advection and diffusion. Our DOC export flux
257 (Fig. 5c) is low in tropical regions, and high in subtropical Atlantic, subtropical north
258 Pacific and high production Subarctic zone, and intermediate in the upwelling Antarctic
259 zone and subtropical south Pacific. Smaller hotspots are also observed in the Peruvian,
260 Mauritanian, Benguela, and Arabian Sea upwelling regions. Our globally integrated DOC
261 export at 114 m is 2.9 (95% CI: 2.4-3.5) Pg C yr⁻¹ (Fig. 3). *Hansell et al.* [2009]

262 estimated a DOC flux of 1.9 Pg C yr^{-1} out of 100 m by considering vertical velocities,
263 mixing coefficients, and DOC concentrations. *Roshan and DeVries* [2017] estimated a
264 global DOC flux from 74 m of $2.31 \pm 0.60 \text{ Pg C yr}^{-1}$. *Letscher et al.* [2015] reported their
265 estimate of $2.28 \text{ Pg C yr}^{-1}$ (25% of the model TOC export flux) from 100 m. Because
266 our DOC includes small non-sinking particles, our estimate is on the high end of previous
267 estimates. It also represents the largest proportion to the total export of organic carbon
268 ever obtained (38% vs 25% respectively).

269 We calculated zonally averaged DOC export proportion (DOC export flux over TOC
270 export flux) for the four biomes (see above section for details) as in *Emerson* [2014].
271 We find that the mean DOC export ratio increases from 24% at equatorial regions, to
272 39% at subtropical regions, and to 50% and 44% at subtropical/subpolar and subpolar
273 regions, respectively. Our poleward increasing DOC export ratios are consistent with
274 the mixed layer pump mechanism [*Dall’Olmo et al.*, 2016; *Gardner et al.*, 1995]. The
275 mixed layer pump invokes diurnal and/or seasonal variation of the mixed layer depth as
276 a mechanism for exporting DOC or small non-sinking particles [*Dall’Olmo et al.*, 2016;
277 *Gardner et al.*, 1995]. Deepening of the mixed layer brings DOC below the euphotic zone,
278 subsequent mixed layer shoaling due to restratification by warming isolates DOC at depth.
279 High latitude oceans experiencing the large seasonality are expected to have the strongest
280 mixed layer pump [*Dall’Olmo et al.*, 2016].

281 Our DOC export flux pattern is quite similar to the net DOC removal rate (equivalent
282 to DOC export flux) estimated based on the U.S. Climate Variability and Predictabil-
283 ity (CLIVAR) DOC observations *Hansell et al.* [2012]. For example, both show DOC
284 export flux is the highest in the subtropical north Atlantic, high in subantarctic ocean,

low/intermediate in the Antarctic zone, low in tropical oceans. Our results are also consistent with *Roshan and DeVries* [2017] in the tropical oceans, the Atlantic Ocean, and the subtropical north Pacific. However, our estimated fluxes show a strikingly different pattern in the Southern Ocean and in upwelling regions (Fig. 5c and Fig. 2b of *Roshan and DeVries* [2017]). *Roshan and DeVries* [2017] extrapolate DOC concentrations mostly sampled during the summer season to the global ocean by applying an artificial neural network (ANN) reconstruction method, which is trained using annually-averaged climatological means of temperature, salinity, oxygen, and nutrient data. They then diagnose the DOC production rate and export flux by coupling the reconstructed DOC concentration field to a global ocean circulation model. One major limitation of their method is that the DOC concentration data used to train the neural network is mostly from summertime field measurements which biases the estimated export in regions with a strong seasonal cycle. While ^{234}Th measurements used in this study were taken from different seasons (Table A1). We hypothesize that both the similarities and differences between our model and that of *Roshan and DeVries* [2017] can be explained by the sampling bias. First, the agreement in the tropical oceans is due to the weak seasonality in low latitudes, reducing the bias induced by applying summer time values for the annual average. Second, the similarity in the North Atlantic Ocean is due to the fact that in that basin, unlike the rest of the ocean, the sampling frequency is high enough to resolve the seasonal cycle. Third, the difference in the Southern Ocean can again be attributed to the presence of a strong and poorly resolved seasonal cycle, although poor spatial resolution might also be a contributor (Fig. 1 of *Roshan and DeVries* [2017]).

3.5. C:P ratios

307 With the optimal b values and an assumed particle dissolution rate constant, one can
308 estimate particle sinking velocity [Kriest and Oschlies, 2008], with which POP sinking flux
309 can be calculated given the POP distribution from the P cycle model (Fig. 1). We have
310 POC flux diagnosed from ^{234}Th flux and $R_{\text{POC}:^{234}\text{Th}}$ ratio. We then compute C:P ratio
311 of sinking particles for each region reported in Teng *et al.* [2014]. C:P ratio of dissolved
312 organic matter is the ratio between DOC and DOP fluxes (Table 1).

313 Geographically, C:P ratio for both particulate and dissolved organic matter is high in
314 subtropical gyres, and low in the Southern Ocean and equatorial upwelling regions. The
315 North Atlantic gyre displays the highest C:P ratio in both dissolved and particulate fluxes.
316 Another noticeable feature is that the the C:P ratio in the flux of dissolved organic matter
317 is higher than in the flux from particles. This is in agreement with the finding of Letscher
318 *et al.* [2015]. In addition, our C:P ratio is highly consistent to the ones estimated in
319 Letscher and Moore [2015] with strongly overlapping errorbars (Table 1).

3.6. Ecological implications

320 Our results shed light on the conundrum of the low POC export in high production re-
321 gions. The export efficiency calculated based on in-situ measurements of primary produc-
322 tion and POC export flux [Maiti *et al.*, 2013] contradicts the empirical relationships that
323 relate the ef-ratio to temperature and total primary production [Laws *et al.*, 2011, 2000].
324 Ecologically, four hypotheses are proposed to explain the occurrence of low particle export
325 in high PP regions [Le Moigne *et al.*, 2016; Laws and Maiti, 2019]:

- 326 • H1 Primary production (PP) is exported not only as particles but also as DOC,

327 • H2 Strong surface microbial recycling even in low temperature regions,
328 • H3 Grazing-mediated export that varies inversely with PP (low grazing in high PP,
329 so virtually no zooplankton mediated export).

330 • H4 A time lag between primary production and export at the base of euphotic zone.

331 For a given PP, these processes (acting individually or together) all decrease the amount
332 of POC exported gravitationally. This could explain why high ef-ratios are very rarely
333 observed in highly productive regions.

334 At the Station ALOHA, the negative relationship disappears when primary production
335 and export were averaged over a long time frame (H4) [*Laws and Maiti, 2019*]. In the
336 Southern Ocean, the observed low export efficiency may be explained by H2 and H3
337 [*Le Moigne et al., 2016*]. However, our high/intermediate DOC export flux in the Southern
338 Ocean indicates that H1 may also be an explanation for the low POC export efficiency
339 observed here. The different conclusions between our model and *Le Moigne et al. [2016]*
340 could be explained by the fact that *Le Moigne et al. [2016]* only examined the diffusive flux
341 of DOC in summer when the water column is stratified while our model provides an annual
342 average. We therefore hypothesize that in addition to surface microbial recycling and
343 grazing-mediated export, which may dominate in summer only, on the annual scale, the
344 export of DOC may be an important process during observed high productivity low export
345 regimes. Elsewhere, in the eastern equatorial Pacific, there are also DOC export hotspots
346 (Fig. 5c). This may indicate that H2 (microbial remineralization of carbon in the surface
347 ocean) prevails in these high productivity warm waters. H3 has yet to be tested in warm
348 high PP regions; however, global distribution of macrozooplankton abundance/biomass
349 indicates that zooplankton stocks are not necessarily different in those regions relative to

350 the adjacent low PP warm waters [*Moriarty et al.*, 2013]. This indicates that H3 may not
351 prevail in warm high PP regions. Our results suggest that that the causes of low POC
352 export in high productivity regimes are not unique, and that they may vary regionally
353 and seasonally. Most global carbon export models and algorithms do not account for the
354 export of DOC [*Guidi et al.*, 2015; *Laws et al.*, 2000; *Siegel et al.*, 2014]. The contribution
355 from DOC is typically included by simply adding an assumed portion to POC export
356 flux [e.g. *Henson et al.*, 2011]. However, *Emerson* [2014] found that POC export is
357 only a small fraction of ANCP at three time series stations. A better understanding of
358 the various pathways associated to the gravitational biological carbon pump should help
359 decipher what controls the efficiency and the magnitude of carbon export [*Cavan et al.*,
360 2015; *Laurenceau-Cornec et al.*, 2015; *Le Moigne et al.*, 2016]. Given the importance of
361 the annual DOC export flux in certain regions (Fig. 5c) relative to the gravitational flux,
362 we suggest that DOC export flux should also be included in future effort to model the
363 global strength of the biological carbon pump, and that algorithm potentially considering
364 DOC export flux need more development.

365 Our results have multiple implications to the global marine carbon cycle. First, a large
366 percentage of carbon is exported in the form of DOC in high latitude oceans. Future
367 global warming is expected to further stratify the ocean and weaken ocean mixing, thus
368 a decreased DOC export flux is expected for the high latitude oceans. If DOC export
369 reduces, other mechanisms such as microbial remineralization in the surface ocean may
370 become dominant factors. Surface DOC recycling will retain nutrients and carbon in the
371 upper ocean, and thus decrease the potential role of the ocean as a global carbon sink.
372 Second, a low POC export rate is found in the subtropical oceans. Future expansion

373 of these regions due to global warming will also decrease gravitational carbon export.
374 However, this reduction may be compensated or even overcome by the higher C:P ratios
375 in the gyres. Lastly, on an annual basis, a large fraction of primary production is exported
376 via DOC with higher C:P ratios compared to POC, which offers a possible explanation
377 for the observed low POC export (relative to the observed NPP) in high latitude oceans.

378 **Acknowledgments.** We sincerely thank all GEOTRACES scientists who made re-
379 lated data available. We appreciate the financial support provided by the Division of
380 Ocean Sciences of the US National Science Foundation (OCE-1436922). W.-L. Wang,
381 R.T.L., F.W.P. and J.K.M. also acknowledge support from the US Department of Energy
382 Office of Biological and Environmental Research (DE-SC0016539). Le M. acknowledge
383 support by a DFG Fellowship of the Excellence Cluster The Future Ocean (CP1403 to
384 F.A.C.L.M.). The code for the inverse model and carbon export flux data are available at
385 DOI: 10.5281/zenodo.2651656. The ^{234}Th data used to constrain the model is from the
386 cited sources (Table A1) and GEOTRACES website: <https://www.geotraces.org>. The
387 DIP data is from World Ocean Atlas 2013 [*Zweng et al.*, 2013; *Garcia et al.*, 2014].

Competing Interests:

388 The authors declare that they have no competing financial interests.

References

- 389 Alldredge, A. L., U. Passow, and B. E. Logan (1993), The abundance and significance of
390 a class of large, transparent organic particles in the ocean, *Deep Sea Research Part I:
391 Oceanographic Research Papers*, *40*(6), 1131–1140.
- 392 Archer, D., A. Winguth, D. Lea, and N. Mahowald (2000), What caused the
393 glacial/interglacial atmospheric pCO₂ cycles?, *Rev. Geophys.*, *38*(2), 159–189.
- 394 Black, E. E., K. O. Buesseler, S. M. Pike, and P. J. Lam (2018), ²³⁴Th as a tracer
395 of particulate export and remineralization in the southeastern tropical Pacific, *Mar.
396 Chem.*, *201*, 35–50.
- 397 Boyd, P. W., H. Claustre, M. Levy, D. A. Siegel, and T. Weber (2019), Multi-faceted
398 particle pumps drive carbon sequestration in the ocean, *Nature*, *568*(7752), 327.
- 399 Britten, G. L., and F. W. Primeau (2016), Biome-specific scaling of ocean productivity,
400 temperature, and carbon export efficiency, *Geophys. Res. Lett.*, *43*(10), 5210–5216.
- 401 Buesseler, K. O. (1998), The decoupling of production and particulate export in the
402 surface ocean, *Global Biogeochem. Cycles*, *12*(2), 297–310.
- 403 Buesseler, K. O., M. P. Bacon, J. K. Cochran, and H. D. Livingston (1992), Carbon and
404 nitrogen export during the JGOFS North Atlantic bloom experiment estimated from
405 ²³⁴Th:²³⁸U disequilibria, *Deep-Sea Res. I.*, *39*(7/8), 1115–1137.
- 406 Buesseler, K. O., J. A. Andrews, M. C. Hartman, R. Belostock, and F. Chai (1995), Re-
407 gional estimates of the export flux of particulate organic carbon derived from thorium-
408 ²³⁴Th during the JGOFS EqPac program, *Deep-Sea Res. II*, *42*(2-3), 777–804.
- 409 Buesseler, K. O., J. Andrews, S. M. Pike, M. A. Charette, L. E. Goldson, M. A. Brzezinski,
410 and V. Lance (2005), Particle export during the Southern Ocean iron experiment

- 411 (SOFeX), *Limnol. Oceanogr.*, *50*(1), 311–327.
- 412 Buesseler, K. O., C. R. Benitez-Nelson, S. Moran, A. Burd, M. Charette, J. K. Cochran,
413 L. Coppola, N. Fisher, S. Fowler, W. Gardner, et al. (2006), An assessment of particulate
414 organic carbon to thorium-234 ratios in the ocean and their impact on the application
415 of ^{234}Th as a POC flux proxy, *Mar. Chem.*, *100*(3-4), 213–233.
- 416 Buesseler, K. O., C. Lamborg, P. Cai, R. Escoube, R. Johnson, S. Pike, P. Masque,
417 D. McGillicuddy, and E. Verdeny (2008), Particle fluxes associated with mesoscale ed-
418 dies in the Sargasso Sea, *Deep-Sea Res. II*, *55*(10-13), 1426–1444.
- 419 Buesseler, K. O., S. Pike, K. Maiti, C. H. Lamborg, D. A. Siegel, and T. W. Trull (2009),
420 Thorium-234 as a tracer of spatial, temporal and vertical variability in particle flux in
421 the North Pacific, *Deep-Sea Res. I*, *56*(7), 1143–1167.
- 422 Cai, P., W. Chen, Z. M. Dai, D. Wan, Q. Wang, T. Li, Tang, and D. Lv (2008), A high-
423 resolution study of particle export in the southern South China Sea based on ^{234}Th : ^{238}U
424 disequilibrium, *J. Geophys. Res.*, *113*(C04019).
- 425 Cai, P., M. Rutgers van der Loeff, I. Stimac, E. M. Nthig, K. Lepore, and S. B. Moran
426 (2010), Low export flux of particulate organic carbon in the central Arctic Ocean as
427 revealed by ^{234}Th ^{238}U disequilibrium, *J. Geophys. Res.*, *115*(C10).
- 428 Cavan, E., F. A. Le Moigne, A. Poulton, G. Tarling, P. Ward, C. Daniels, G. Fragoso,
429 and R. Sanders (2015), Attenuation of particulate organic carbon flux in the scotia sea,
430 southern ocean, is controlled by zooplankton fecal pellets, *Geophys. Res. Lett.*, *42*(3),
431 821–830.
- 432 Charette, M. A., S. B. Moran, and J. K. Bishop (1999), ^{234}Th as a tracer of particulate
433 organic carbon export in the subarctic northeast Pacific Ocean, *Deep-Sea Res. II*, *46*(11-

- 434 12), 2833–2861.
- 435 Cochran, J. K., K. O. Buesseler, M. P. Bacon, H. W. Wang, D. J. Hirschberg, L. Ball,
436 J. Andrews, G. Crossin, and A. Fler (2000), Short-lived thorium isotopes (^{234}Th , ^{238}Th)
437 as indicators of POC export and particle cycling in the Ross Sea, Southern Ocean, *Deep-*
438 *Sea Res. II*, *47*, 3451–3490.
- 439 Coppola, L., M. Roy-Barman, S. Mulsow, P. Povinec, and C. Jeandel (2005), Low partic-
440 ulate organic carbon export in the frontal zone of the Southern Ocean (Indian sector)
441 revealed by ^{234}Th , *Deep-Sea Res. I*, *52*(1), 51–68.
- 442 Dall’Olmo, G., J. Dingle, L. Polimene, R. J. Brewin, and H. Claustre (2016), Substantial
443 energy input to the mesopelagic ecosystem from the seasonal mixed-layer pump, *Nat.*
444 *Geosci.*, *9*(11), 820–823.
- 445 DeVries, T., and F. W. Primeau (2011), Dynamically and observationally constrained
446 estimates of water-mass distributions and ages in the global ocean, *J. Phys. Oceanogr.*,
447 *41*(12), 2381–2401.
- 448 Dunne, J. P., R. A. Armstrong, A. Gnanadesikan, and J. L. Sarmiento (2005), Empirical
449 and mechanistic models for the particle export ratio, *Global Biogeochem. Cycles*, *19*(4).
- 450 Emerson, S. (2014), Annual net community production and the biological carbon flux in
451 the ocean, *Global Biogeochem. Cycles*, *28*(1), 14–28.
- 452 Eppley, R. W., and B. J. Peterson (1979), Particulate organic matter flux and planktonic
453 new production in the deep ocean, *Nature*, *282*(5740), 677.
- 454 Fu, W., and F. Primeau (2017), Application of a fast Newton–Krylov solver for equilibrium
455 simulations of phosphorus and oxygen, *Ocean Model.*, *119*, 35–44.

- 456 Galbraith, E. D., and A. C. Martiny (2015), A simple nutrient-dependence mechanism for
457 predicting the stoichiometry of marine ecosystems, *Proc. Natl. Acad. Sci. USA*, *112*(27),
458 8199–8204.
- 459 Garcia, H., R. Locarnini, T. Boyer, J. Antonov, O. Baranova, M. Zweng, J. Reagan, and
460 D. Johnson (2014), World Ocean Atlas 2013, Volume 4: Dissolved Inorganic Nutrients
461 (Phosphate, Nitrate, Silicate), NOAA Atlas NESDIS, vol. 76, edited by S. Levitus, 25
462 pp, *US Gov. Print. Off., Washington, DC*.
- 463 Gardner, W. D., S. P. Chung, M. J. Richardson, and I. D. Walsh (1995), The oceanic
464 mixed-layer pump, *Deep-Sea Res. II*, *42*(2-3), 757–775.
- 465 Giering, S. L., R. Sanders, R. S. Lampitt, T. R. Anderson, C. Tamburini, M. Boutrif,
466 M. V. Zubkov, C. M. Marsay, S. A. Henson, K. Saw, et al. (2014), Reconciliation of the
467 carbon budget in the oceans twilight zone, *Nature*, *507*(7493), 480.
- 468 Guidi, L., L. Legendre, G. Reygondeau, J. Uitz, L. Stemann, and S. A. Henson (2015),
469 A new look at ocean carbon remineralization for estimating deepwater sequestration,
470 *Global Biogeochem. Cycles*, *29*(7), 1044–1059.
- 471 Hansell, D. A., C. A. Carlson, D. J. Repeta, and R. Schlitzer (2009), Dissolved organic
472 matter in the ocean: A controversy stimulates new insights, *Oceanography*, *22*(4), 202–
473 211.
- 474 Hansell, D. A., C. A. Carlson, and R. Schlitzer (2012), Net removal of major marine
475 dissolved organic carbon fractions in the subsurface ocean, *Global Biogeochem. Cycles*,
476 *26*(1).
- 477 Harrison, C. S., M. C. Long, N. S. Lovenduski, and J. K. Moore (2018), Mesoscale effects
478 on carbon export: A global perspective, *Global Biogeochem. Cycles*, *32*(4), 680–703.

- 479 Henson, S. A., R. Sanders, E. Madsen, P. J. Morris, F. Le Moigne, and G. D. Quartly
480 (2011), A reduced estimate of the strength of the ocean’s biological carbon pump,
481 *Geophys. Res. Lett.*, *38*(4).
- 482 Henson, S. A., R. Sanders, and E. Madsen (2012), Global patterns in efficiency of partic-
483 ulate organic carbon export and transfer to the deep ocean, *Global Biogeochem. Cycles*,
484 *26*(1).
- 485 KawaKami, H., M. C. Honda, K. Matsumoto, T. Fujiki, and S. Watanabe (2010), East-
486 west Distribution of POC fluxes estimated from ^{234}Th in the northern North Pacific in
487 Autumn, *J. oceanogr.*, *66*, 71–83.
- 488 Kriest, I., and A. Oschlies (2008), On the treatment of particulate organic matter sinking
489 in large-scale models of marine biogeochemical cycles, *Biogeosciences (BG)*, *5*, 55–72.
- 490 Kwon, E. Y., F. Primeau, and J. L. Sarmiento (2009), The impact of remineralization
491 depth on the air–sea carbon balance, *Nat. Geosci.*, *2*(9), 630.
- 492 Lalande, C., S. B. Moran, P. Wassmann, J. M. Grebmeier, and L. W. Cooper (2008),
493 ^{234}Th -derived particulate organic carbon fluxes in the northern Barents Sea with com-
494 parison to drifting sediment trap fluxes, *J. Marine Syst.*, *73*(1-2), 103–113.
- 495 Lam, P. J., and J. K. Bishop (2007), High biomass, low export regimes in the southern
496 ocean, *Deep-Sea Res. II*, *54*(5-7), 601–638.
- 497 Laurenceau-Cornec, E. C., T. W. Trull, D. M. Davies, S. G. Bray, J. Doran, F. Planchon,
498 F. Carlotti, M.-P. Jouandet, A.-J. Cavagna, A. M. Waite, and S. Blain (2015), The
499 relative importance of phytoplankton aggregates and zooplankton fecal pellets to carbon
500 export: insights from free-drifting sediment trap deployments in naturally iron-fertilised
501 waters near the Kerguelen Plateau, *Biogeosciences*, *12*(4), 1007–1027.

- 502 Laws, E. A., and K. Maiti (2019), The relationship between primary production and
503 export production in the ocean: Effects of time lags and temporal variability, *Deep-Sea*
504 *Res. I*, 148, 100–107.
- 505 Laws, E. A., P. G. Falkowski, W. O. Smith, H. Ducklow, and J. J. McCarthy (2000),
506 Temperature effects on export production in the open ocean, *Global Biogeochem. Cycles*,
507 14(4), 1231–1246.
- 508 Laws, E. A., E. D’Sa, and P. Naik (2011), Simple equations to estimate ratios of new
509 or export production to total production from satellite-derived estimates of sea surface
510 temperature and primary production, *Limnol. Oceanogr. Methods*, 9(12), 593–601.
- 511 Le Moigne, F., A. J. Poulton, S. A. Henson, C. J. Daniels, G. M. Fragoso, E. Mitchell,
512 S. Richier, B. C. Russell, H. E. Smith, G. A. Tarling, et al. (2015), Carbon export
513 efficiency and phytoplankton community composition in the Atlantic sector of the Arctic
514 Ocean, *J. Geophys. Res. Oceans*, 120(6), 3896–3912.
- 515 Le Moigne, F. A., C. M. Moore, R. J. Sanders, M. Villa-Alfageme, S. Steigenberger, and
516 E. P. Achterberg (2014), Sequestration efficiency in the iron-limited North Atlantic:
517 Implications for iron supply mode to fertilized blooms, *Geophys. Res. Lett.*, 41(13),
518 4619–4627.
- 519 Le Moigne, F. A., S. A. Henson, E. Cavan, C. Georges, K. Pabortsava, E. P. Achterberg,
520 E. Ceballos-Romero, M. Zubkov, and R. J. Sanders (2016), What causes the inverse
521 relationship between primary production and export efficiency in the Southern Ocean?,
522 *Geophys. Res. Lett.*, 43(9), 4457–4466.
- 523 Le Moigne, F. A. C., S. A. Henson, R. J. Sanders, and E. Madsen (2013), Global database
524 of surface ocean particulate organic carbon export fluxes diagnosed from the ^{234}Th

- 525 technique, *Earth Syst. Sci. Data*, 5(2), 295–304.
- 526 Letscher, R., J. Moore, Y. Teng, and F. Primeau (2015), Variable C: N: P stoichiometry
527 of dissolved organic matter cycling in the Community Earth System Model, *Biogeo-*
528 *sciences*, 12(1), 209.
- 529 Letscher, R. T., and J. K. Moore (2015), Preferential remineralization of dissolved organic
530 phosphorus and non-redfield dom dynamics in the global ocean: Impacts on marine
531 productivity, nitrogen fixation, and carbon export, *Global Biogeochem. Cycles*, 29(3),
532 325–340.
- 533 Maiti, K., M. A. Charette, K. O. Buesseler, and M. Kahru (2013), An inverse relationship
534 between production and export efficiency in the Southern Ocean, *Geophys. Res. Lett.*,
535 40(8), 1557–1561.
- 536 Martin, J. H., G. A. Knauer, D. M. Karl, and W. W. Broenkow (1987), VERTEX: carbon
537 cycling in the Northeast Pacific, *Deep-Sea Res. I*, 34(2), 267–285.
- 538 Mawji, E., R. Schlitzer, E. M. Dodas, C. Abadie, W. Abouchami, R. F. Anderson,
539 O. Baars, K. Bakker, M. Baskaran, N. R. Bates, et al. (2015), The geotraces inter-
540 mediate data product 2014.
- 541 Moriarty, R., E. Buitenhuis, C. L. Quéré, and M.-P. Gosselin (2013), Distribution of
542 known macrozooplankton abundance and biomass in the global ocean, *Earth Syst. Sci.*
543 *Data*, 5(2), 241–257.
- 544 Mouw, C. B., A. Barnett, G. A. McKinley, L. Gloege, and D. Pilcher (2016), Global ocean
545 particulate organic carbon flux merged with satellite parameters, *Earth Syst. Sci. Data*,
546 8(2), 531.

- 547 Owens, S. A., K. O. Buesseler, and K. W. W. Sims (2011), Re-evaluating the ^{238}U -salinity
548 relationship in seawater: Implications for the $^{238}\text{U}^{234}\text{Th}$ disequilibrium method, *Mar.*
549 *Chem.*, *127*(1-4), 31–39.
- 550 Owens, S. A., S. Pike, and K. O. Buesseler (2015), Thorium-234 as a tracer of particle
551 dynamics and upper ocean export in the Atlantic Ocean, *Deep-Sea Res. II*, *116*, 42–59.
- 552 Planchon, F., A.-J. Cavagna, D. Cardinal, L. A. , and F. Dehairs (2013), Late summer
553 particulate organic carbon export and twilight zone remineralisation in the Atlantic
554 sector of the Southern Ocean, *Biogeosciences*, *10*, 803–820.
- 555 Planchon, F., D. Ballas, A. Cavagna, A. Bowie, D. Davies, T. Trull, E. Laurenceau-
556 Cornec, P. Van Der Merwe, and F. Dehairs (2015), Carbon export in the naturally
557 iron-fertilized Kerguelen area of the Southern Ocean based on the ^{234}Th approach,
558 *Biogeosciences*, *12*(12), 3831–3848.
- 559 Primeau, F. W., M. Holzer, and T. DeVries (2013), Southern Ocean nutrient trapping
560 and the efficiency of the biological pump, *J. Geophys. Res. Ocean.*, *118*(5), 2547–2564.
- 561 Roca-Martí, M., V. Puigcorbé, M. H. Iversen, M. R. van der Loeff, C. Klaas, W. Cheah,
562 A. Bracher, and P. Masqué (2017), High particulate organic carbon export during the
563 decline of a vast diatom bloom in the Atlantic sector of the Southern Ocean, *Deep-Sea*
564 *Res. II*, *138*, 102–115.
- 565 Rosengard, S. Z., P. J. Lam, W. M. Balch, M. E. Auro, S. Pike, D. Drapeau, and B. Bowler
566 (2015), Carbon export and transfer to depth across the Southern Ocean Great Calcite
567 Belt, *Biogeosciences*, *12*(13), 3953–3971.
- 568 Roshan, S., and T. DeVries (2017), Efficient dissolved organic carbon production and
569 export in the oligotrophic ocean, *Nat. Commun.*, *8*(1), 2036.

570 Rutgers van der Loeff, M., J. Friedrich, and U. V. Bathmann (1997), Carbon export
571 during the Spring Bloom at the Antarctic Polar Front, determined with the natural
572 tracer ^{234}Th , *Deep-Sea Res. II*, *44*(1-2), 457–478.

573 Rutgers van der Loeff, M., P. H. Cai, I. Stimac, A. Bracher, R. Middag, M. B. Klunder,
574 and S. M. A. C. van Heuven (2011), ^{234}Th in surface waters: Distribution of particle
575 export flux across the Antarctic Circumpolar Current and in the Weddell Sea during the
576 GEOTRACES expedition ZERO and DRAKE, *Deep-Sea Res. II*, *58*(25-26), 2749–2766.

577 Santschi, P., L. Guo, I. Walsh, M. Quigley, and M. Baskaran (1999), Boundary exchange
578 and scavenging of radionuclides in continental margin waters of the Middle Atlantic
579 Bight: implications for organic carbon fluxes, *Cont. Shelf Res.*, *19*, 609–636.

580 Savoye, N., C. Benitez-Nelson, A. B. Burd, J. K. Cochran, M. Charette, K. O. Buesseler,
581 G. A. Jackson, M. Roy-Barman, S. Schmidt, and M. Elskens (2006), ^{234}Th sorption and
582 export models in the water column: A review, *Mar. Chem.*, *100*(3-4), 234–249.

583 Schlitzer, R., R. F. Anderson, E. M. Dodas, M. Lohan, W. Geibert, A. Tagliabue,
584 A. Bowie, C. Jeandel, M. T. Maldonado, W. M. Landing, et al. (2018), The GEO-
585 TRACES Intermediate Data Product 2017, *Chem. Geol.*, *493*, 210–223.

586 Siegel, D. A., K. O. Buesseler, S. C. Doney, S. F. Sailley, M. J. Behrenfeld, and P. W. Boyd
587 (2014), Global assessment of ocean carbon export by combining satellite observations
588 and food-web models, *Global Biogeochem. Cycles*, *28*(3), 181–196.

589 Teng, Y. C., F. W. Primeau, J. K. Moore, M. W. Lomas, and A. C. Martiny (2014),
590 Global-scale variations of the ratios of carbon to phosphorus in exported marine organic
591 matter, *Nat. Geosci.*, *7*(12), 895–898.

- 592 Thomalla, S., R. Turnewitsch, M. Lucas, and A. Poulton (2006), Particulate organic
593 carbon export from the North and South Atlantic gyres: The $^{234}\text{Th}/^{238}\text{U}$ disequilibrium
594 approach, *Deep-Sea Res. II*, 53(14-16), 1629–1648.
- 595 Wang, W.-L., J. K. Moore, A. C. Martiny, and F. W. Primeau (2019a), Convergent
596 estimates of marine nitrogen fixation, *Nature*, 566(7743), 205.
- 597 Wang, W.-L., C. Lee, and F. W. Primeau (2019b), A Bayesian statistical approach to
598 inferring particle dynamics from in-situ pump POC and chloropigment data from the
599 Mediterranean Sea, *Mar. Chem.*, 214, 103,654.
- 600 Westberry, T., M. Behrenfeld, D. Siegel, and E. Boss (2008), Carbon-based primary pro-
601 ductivity modeling with vertically resolved photoacclimation, *Global Biogeochem. Cy-
602 cles.*, 22(2), GB2024.
- 603 Zhou, K., S. D. Nodder, M. Dai, and J. Hall (2012), Insignificant enhancement of export
604 flux in the highly productive subtropical front, east of New Zealand: a high resolution
605 study of particle export fluxes based on ^{234}Th : ^{238}U disequilibria, *Biogeosciences*, 9(3),
606 973–992.
- 607 Zweng, M., J. Reagan, J. Antonov, R. Locarnini, A. Mishonov, T. Boyer, H. Garcia,
608 O. Baranova, D. Johnson, D. Seidov, and M. Biddle (2013), World Ocean Atlas 2013,
609 Volume 2: Salinity, NOAA Atlas NESDIS 74, edited by S. Levitus, 39 pp.

Table 1. Comparison of C:P export ratios to reference values. $(\text{C:P})_P$ is carbon to phosphorus ratio of sinking particles and $(\text{C:P})_D$ is the ratio of dissolved organic matter.

‡ bulk C:P (DOC + POC) ratio from *Teng et al.* [2014].

† This study.

* dissolved C:P ratio from *Letscher and Moore* [2015].

N.A.: not available.

Regions	$(\text{C:P})_{bulk}^{\ddagger}$	$(\text{C:P})_P^{\dagger}$	$(\text{C:P})_D^{\dagger}$	$(\text{C:P})_D^*$
N. Atlantic gyre	355^{+65}_{-59}	159^{181}_{136}	448^{526}_{355}	380 ± 188
Equatorial Atlantic	81^{+21}_{-18}	105^{121}_{89}	191^{243}_{167}	186 ± 29
S. Atlantic gyre	163^{+49}_{-42}	138^{160}_{117}	212^{292}_{150}	130 ± 18
Southern Ocean	91^{+11}_{-9}	105^{121}_{89}	102^{127}_{81}	N.A.
S. Indian gyre	115^{+42}_{-35}	153^{175}_{129}	140^{201}_{106}	N.A.
Equatorial Indian Ocean	103^{+30}_{-26}	112^{130}_{112}	195^{301}_{146}	N.A.
S. Pacific gyre	138^{+37}_{-33}	139^{161}_{118}	171^{255}_{104}	140 ± 121
Equatorial Pacific	83^{+15}_{-13}	104^{120}_{88}	176^{240}_{143}	N.A.
N. Pacific gyre	176^{+33}_{-30}	137^{159}_{116}	283^{356}_{207}	247 ± 15
N. Subpolar Pacific	86^{+23}_{-20}	92^{107}_{78}	127^{172}_{95}	120 ± 33
N. subpolar Atlantic	63^{+24}_{-20}	87^{100}_{74}	97^{127}_{71}	347 ± 33

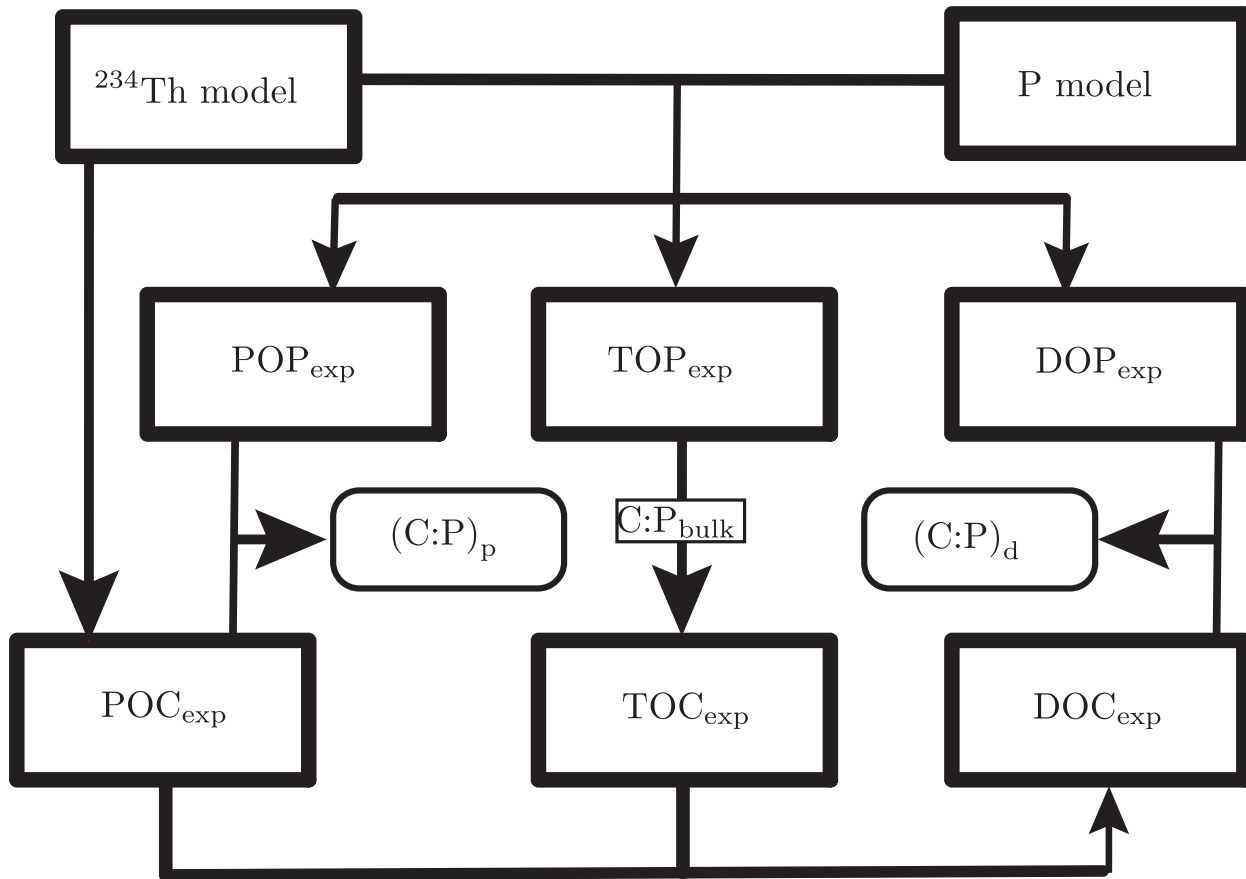


Figure 1. Schematic representation of the joint ^{234}Th and phosphorus model. The model parameters are jointly constrained using observed DIP and ^{234}Th concentration/activity. The black arrows show the flow of information for the calculation of each export component. C:P_{bulk} is bulk C:P export ratio, which is the average of C:P ratios of *Teng et al.* [2014] and *Wang et al.* [2019a].

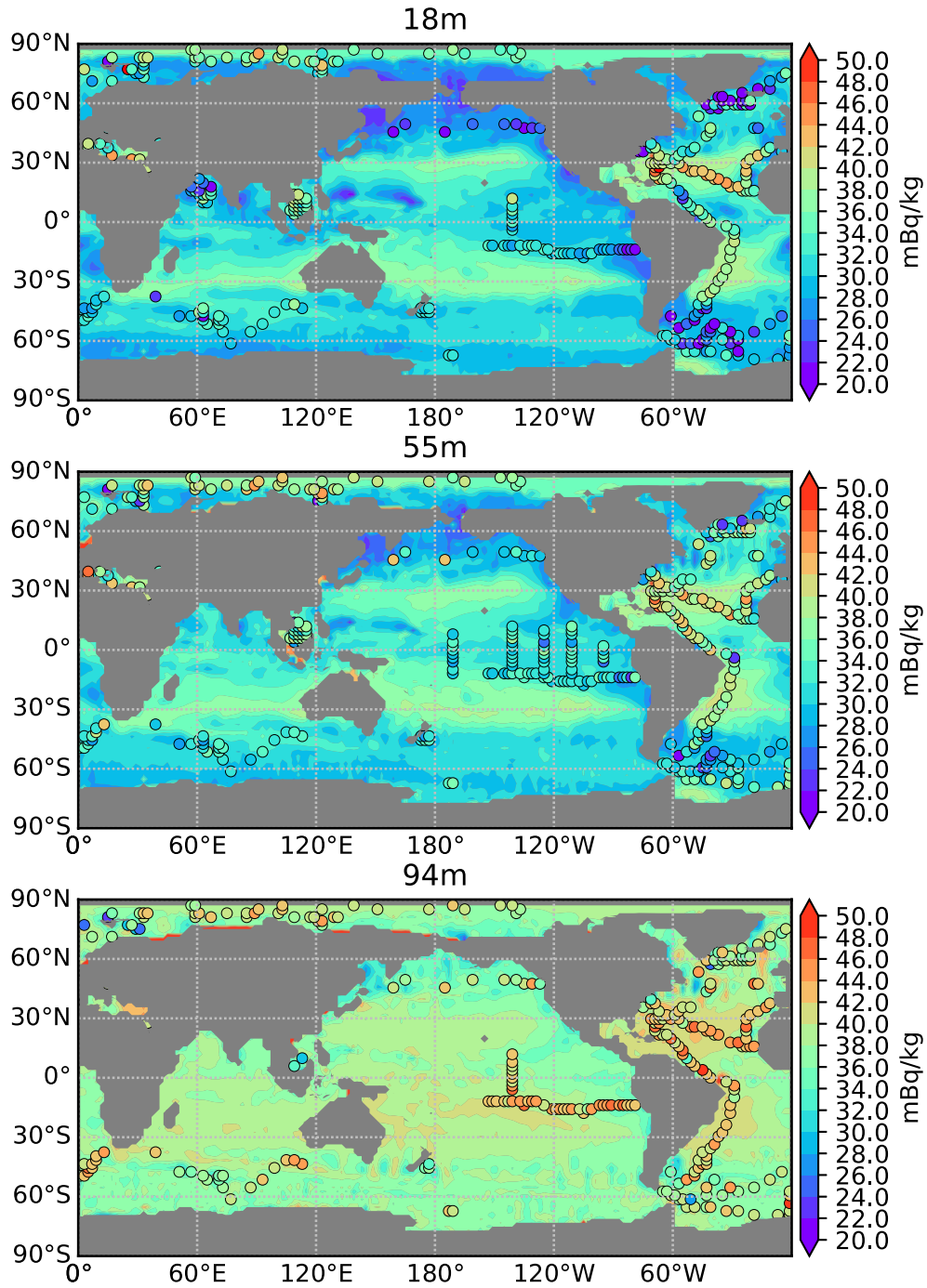


Figure 2. Distribution of total ^{234}Th activity. Total ^{234}Th activity at top three model layers overlaid with in situ observation using the same color scale. See Appendix A for data source.

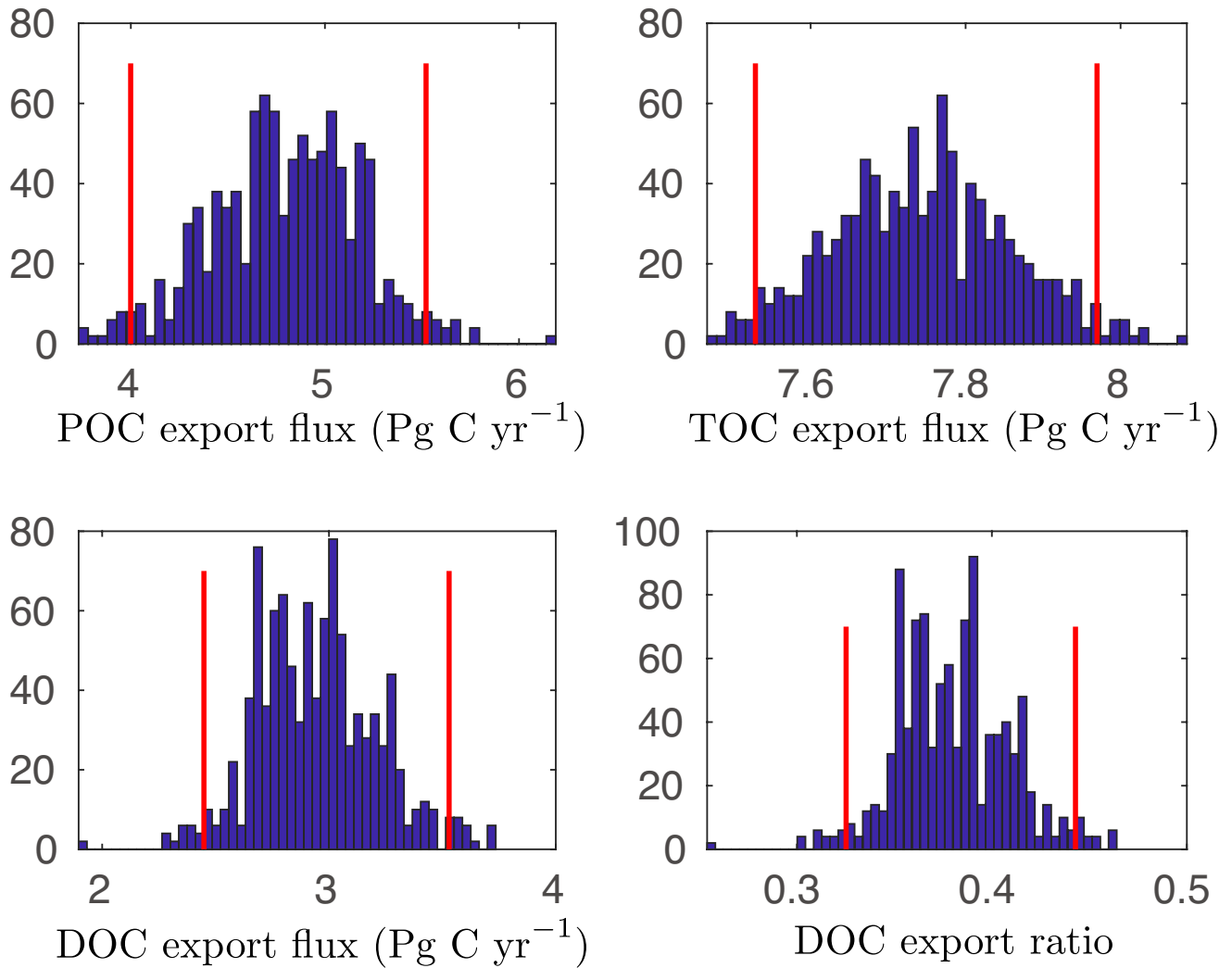


Figure 3. Histogram shows total POC, TOC, and DOC distributions based on Monte Carlo simulation. In the test, we randomly select parameter combinations ($\theta_i \sim N(\hat{\theta}, \Sigma)$), with which we recalculated POC, TOC, and DOC export flux. A sample size of 1000 model runs is shown in the histogram.

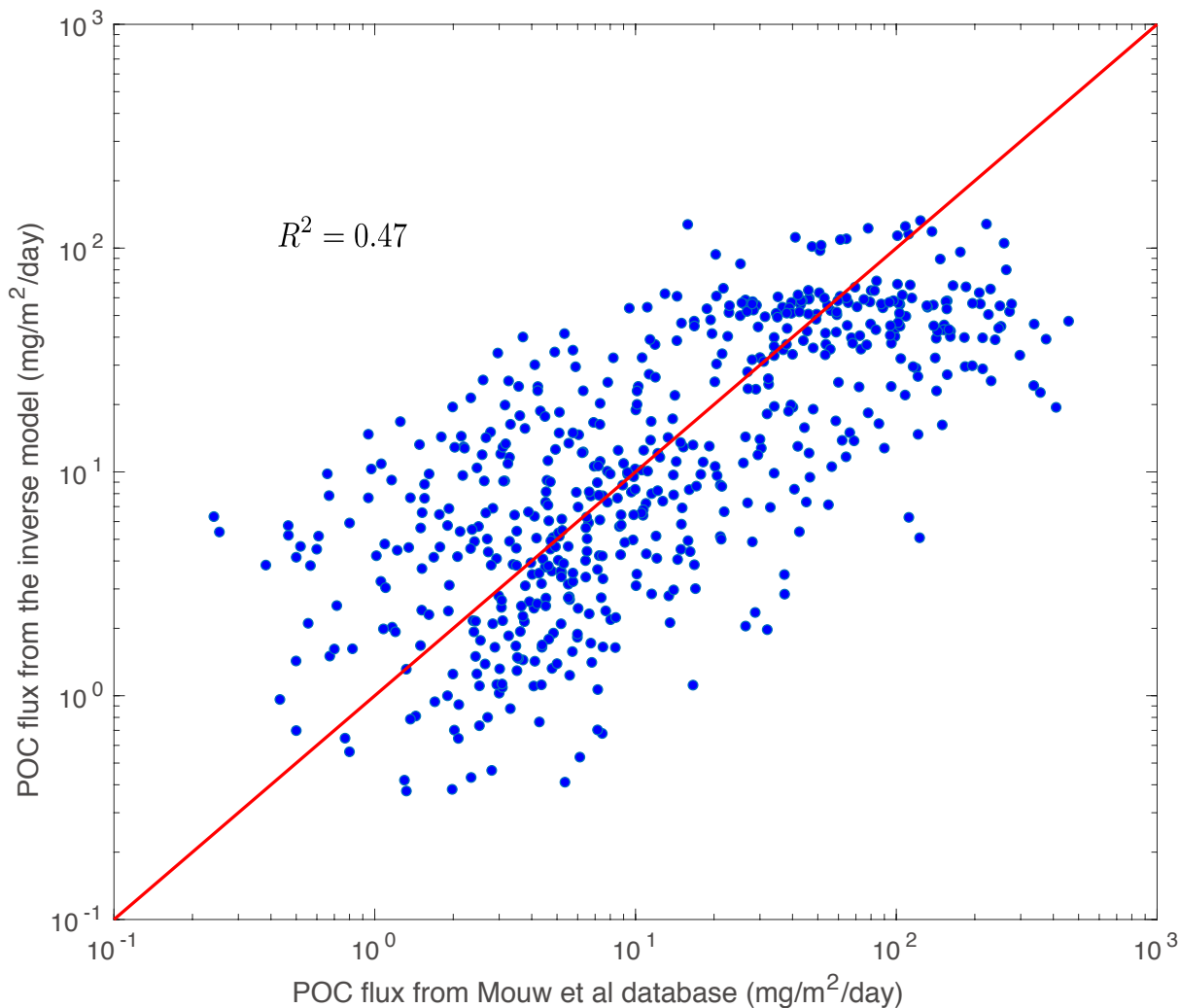


Figure 4. Comparison of model inferred POC flux with *Mouw et al.* [2016], of which 96% were measured using sediment trap, and the other 4% using ^{234}Th method. $R^2 = 0.47$ on log scale. The red line is 1:1 line.

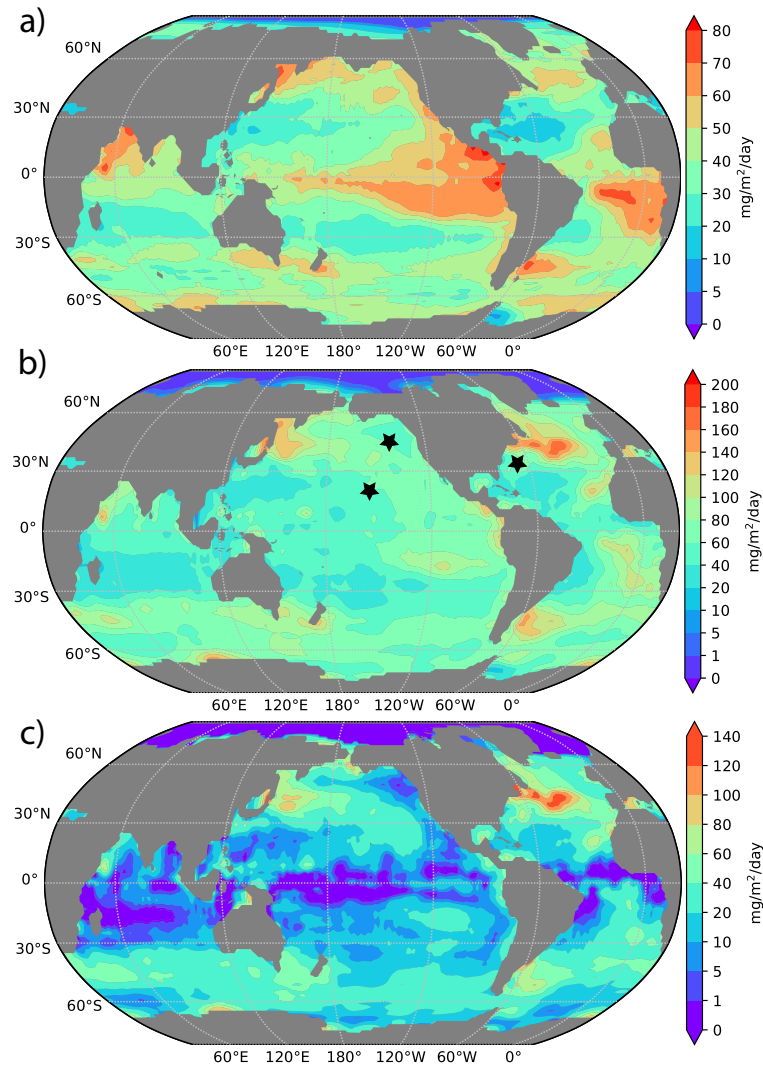


Figure 5. Contour plots of model inferred POC (a) flux at 100 m, TOC (b) and DOC (c) export fluxes at 114 m. POC flux is constrained using model ^{234}Th distribution. Note that the original POC flux is calculated at 114 m because this is the depth of the third grid box. We then scaled POC flux to 100 m using Martin curve function and optimal b values. TOC flux is calculated based on the phosphorus model and spatially varying C:P ratio from *Teng et al.* [2014] and *Wang et al.* [2019a]. The three black dots indicate locations of three time-series sites, Ocean Station Papa (OSP), Hawaii Ocean Time-series (HOT), and Bermuda Atlantic Time-series Study (BATS). DOC export flux is the difference between TOC and POC export fluxes.

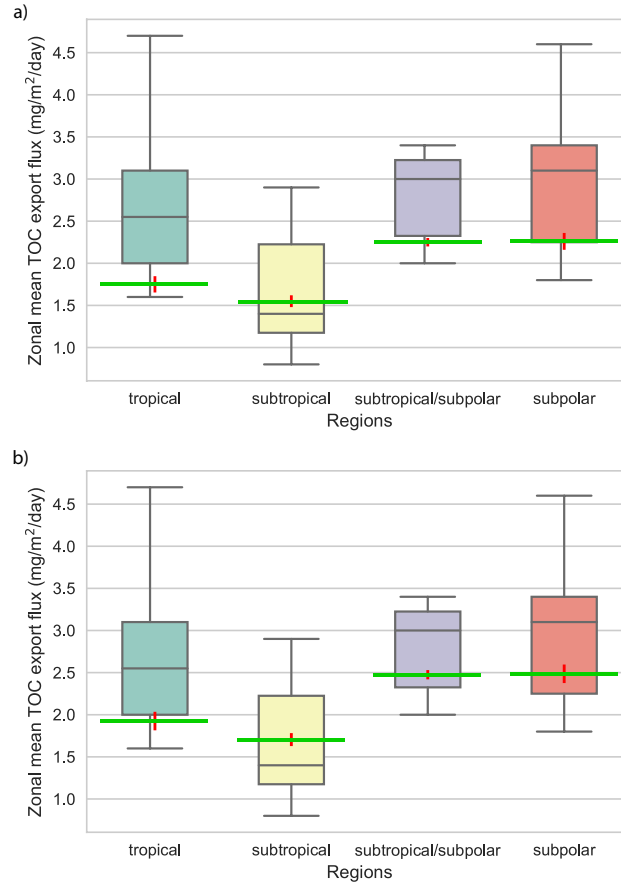


Figure 6. Comparisons of TOC export flux to Annual Net Community Production (ANCP, $\text{mol C m}^{-2} \text{ yr}^{-1}$). ANCP over an annual cycle equals to the flux of biogenic organic matter, TOC export flux in our model. Global ocean is divided into four regions, tropical ($0\text{-}15^\circ$), subtropical ($15\text{-}30^\circ$), subtropical/subpolar ($30\text{-}45^\circ$), and subpolar ($45\text{-}60^\circ$) according to *Emerson* [2014]. The zonally averaged data denoted by the box plots are from Table 1 of *Emerson* [2014]. Boxplots display the 25(Q1), 50(Q2), and 75(Q3) percentiles, the whiskers show the “minimum” and “maximum”, which are defined as $Q1-1.5\text{IQR}$ and $Q3+1.5\text{IQR}$ where IQR is the range from 25(Q1) to 75(Q3) percentile. Flux of figure (a) is at 114 m, and flux of figure (b) is scaled up to 100 m by applying a 10% factor. The blank circles with red errorbars (median with 95% CI) are zonally average value from our model.

Appendix A: Data

Total ^{234}Th (particulate+dissolved) activity are obtained by compiling data from GEOTRACES [Mawji et al., 2015; Schlitzer et al., 2018] and from published reference (Table A1). Globally, we have a total of 3723 measurements from the literature and 2262 from US GEOTRACES. After binning these observations into the grid of the Ocean Circulation Inverse Model (OCIM) ($2^\circ \times 2^\circ$ resolution with 24 vertical levels), there are 2521 grid boxes with ^{234}Th measurements. ^{234}Th based upper ocean (<150 m) POC flux data are from <https://www.pangaea.de/> [Le Moigne et al., 2013], with new data from Black et al. [2018]. The inverse model also uses salinity, phosphate, and net primary production (NPP) data. The salinity and inorganic phosphorus data are from World Ocean Atlas 2013 [Zweng et al., 2013; Garcia et al., 2014]. Net primary production (NPP) data used to parameterize biological phosphate uptake are satellite-derived carbon based primary production data (MODIS CbPM) [Westberry et al., 2008]. Sediment POC flux data are downloaded from <https://doi.pangaea.de/10.1594/PANGAEA.855600> [Mouw et al., 2016], and are binned into the grid of OCIM.

Appendix B: Sensitivity tests

In the model, we use particulate organic phosphorus [POP] as a proxy for sinking particles that carries ^{234}Th out of the surface ocean. We acknowledge that phosphorus is a small portion of sinking particles, other components, such as particulate organic carbon, opal, and calcium carbonate, also absorb dissolved thorium. Here we run multiple sensitivity tests to demonstrate that our model is robust to $R_{M:P}$, sinking mass to phosphorus ratio.

In the first test, we converted POP to POC by applying spatially variable C:P ratios based on Galbraith and Martiny [2015]. We tested if the converted [POC] is a better proxy for the sinking

630 particles because carbon is a larger portion of sinking particles compared to phosphorus. However,
631 we reject this model based on its poor fit to the observation (Fig. A4). One possible reason for
632 the poor performance is that POC may not represent sinking mass better than phosphorus. One
633 can imagine that in high productivity regions, such as the Southern Ocean, the C:P ratio is
634 low [e.g. *Galbraith and Martiny, 2015*], but total sinking mass (sum of organic matter, calcium
635 carbonate and opal etc.) to P ratio can be high because of high diatom activities.

In a second experiment, we formulated two equations for the sinking mass to phosphorus ratio ($R_{M:P}$), in which sinking mass is proportional to the ambient phosphorus concentration. Two parameters controlling the “slope” (S) and “intercept” (R_{min}) are optimized in the inversion.

$$R_{M:P} = R_{min} + S(1 - \tanh([\text{DIP}])), \tag{B1}$$

$$R_{M:P} = R_{min} - S[\text{DIP}].$$

636 We found that the optimal value of R_{min} correlates with the adsorption and desorption rate
637 constants, and the optimal value of S is less than 1×10^{-2} . Thus, we obtain virtually the same
638 POC and DOC export patterns as in the control model. Based on the current data constraints,
639 we did not find evidence indicating that $R_{M:P}$ has significantly spatial variations. The implied
640 gradients are sufficiently weak to be ignored.

Table A1. Sampling time, area, number of samples (N), methods of measurement (Methods), and reference of ^{234}Th data. Sampling time and locations of GEOTRACES samples can be retrieved from the following website: <https://www.geotraces.org>.

Year	Regions	N	Methods	Reference
Oct.-Nov.(1992)	Southern Ocean	124	Part.+Diss.	<i>Rutgers van der Loeff et al.</i> [1997]
Feb. May, Aug. (1996) Feb. (1997)	Subarctic Pacific	161	Part.+Diss.	<i>Charette et al.</i> [1999]
May (1993) Jun-Jul.(1994)	Middle Atlantic Bight	64	Part.+Diss.	<i>Santschi et al.</i> [1999]
Jan.-Feb.(1999)	Southern Ocean	50	Part.+Diss.	<i>Coppola et al.</i> [2005]
Jan.-Feb.(2002)	Southern Ocean	120	Total	<i>Buesseler et al.</i> [2005]
Apr.-May (2004)	Atlantic (50S-50N)	88	Total	<i>Thomalla et al.</i> [2006]
Jul.(2003),May(2005)	Arctic	38	Total	<i>Lalande et al.</i> [2008]
Apr.-May (2004)	South China Sea	174	Total	<i>Cai et al.</i> [2008]
Jun.-Aug.(2004),Jul.-Aug.(2005)	North Atlantic	678	Total	<i>Buesseler et al.</i> [2008]
Sep.-Oct.(2005)	North Pacific	31	Total	<i>KawaKami et al.</i> [2010]
Jul.-Oct.(2007)	Arctic	236	Total	<i>Cai et al.</i> [2010]
Feb.-Mar.(2008)	Southern Ocean	197	Total	<i>Rutgers van der Loeff et al.</i> [2011]
May-Jun. (2008)	South-west Pacific	147	Total	<i>Zhou et al.</i> [2012]
Jan.-Mar.(2008)	Bonus-GoodHope section	175	Total	<i>Planchon et al.</i> [2013]
Oct.-Nov.(2011)	Southern Ocean	185	Total	<i>Planchon et al.</i> [2015]
Austral Summer (2011,2012)	Southern Ocean	318	Total	<i>Rosengard et al.</i> [2015]
Jan.-Feb.(2012)	Southern Ocean	107	Part.+Diss.	<i>Roca-Martí et al.</i> [2017]
2009	North Atlantic	97	Total	<i>Le Moigne et al.</i> [2013]
Jul.-Aug.(2010)	North Atlantic	195	Total	<i>Le Moigne et al.</i> [2014]
Jun.-Jul.(2012)	Arctic	98	Total	<i>Le Moigne et al.</i> [2015]
Jan.-Feb.(2013)	Southern Ocean	127	Total	<i>Le Moigne et al.</i> [2016]

Table A2. Most probable parameter values. κ_d is DOP remineralization rate constant. α and β are the two parameters in the function that scales NPP to DIP assimilation rate (Eq. 2). κ_1 and κ_{-1} are thorium adsorption and desorption rate constant. The optimal b values are displayed in Fig.A1.

Parameters	values	units
κ_d	$(3.78_{-0.05}^{+0.06}) \times 10^{-8}$	s^{-1}
α	$2.50_{-0.20}^{+0.20}$	s^{-1}
β	$0.71_{-0.01}^{+0.01}$	unitless
κ_1	$(2.69_{-0.04}^{+0.04}) \times 10^{-5}$	$m^3 \text{ mmol}^{-1} s^{-1}$
κ_{-1}	$(9.19_{-0.24}^{+0.24}) \times 10^{-7}$	s^{-1}

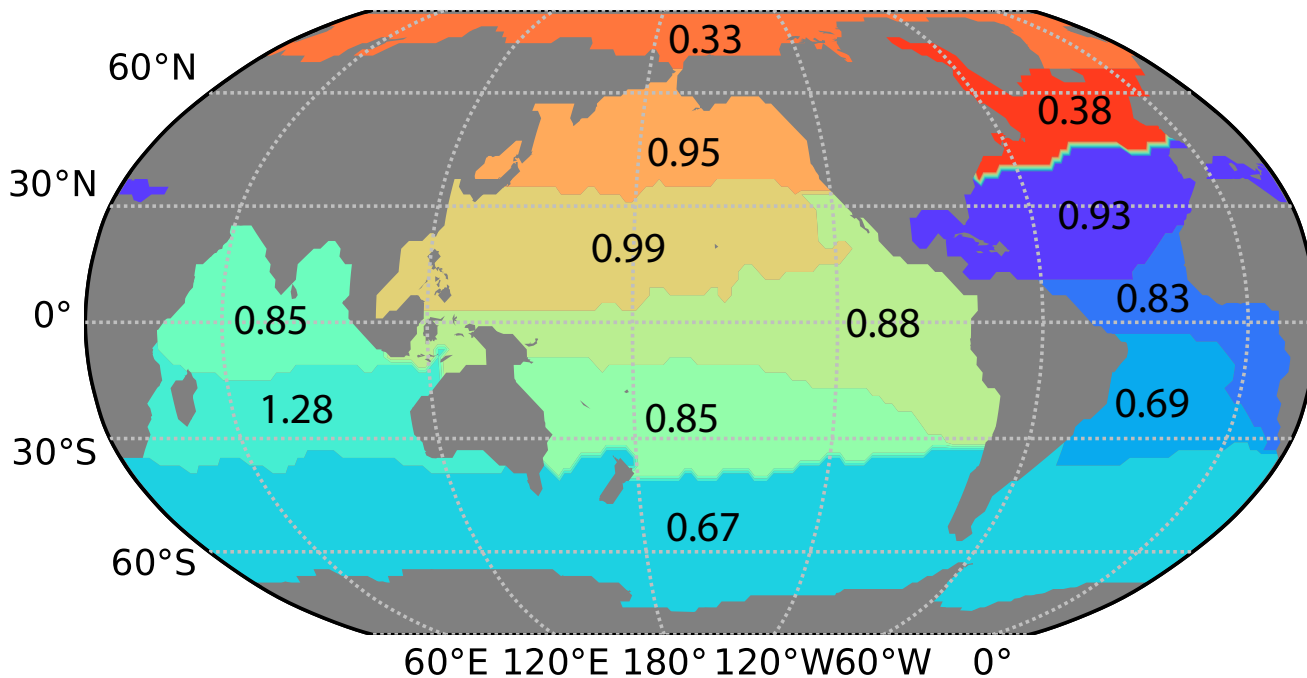


Figure A1. Optimal b values for each region based on *Teng et al.* [2014] division.

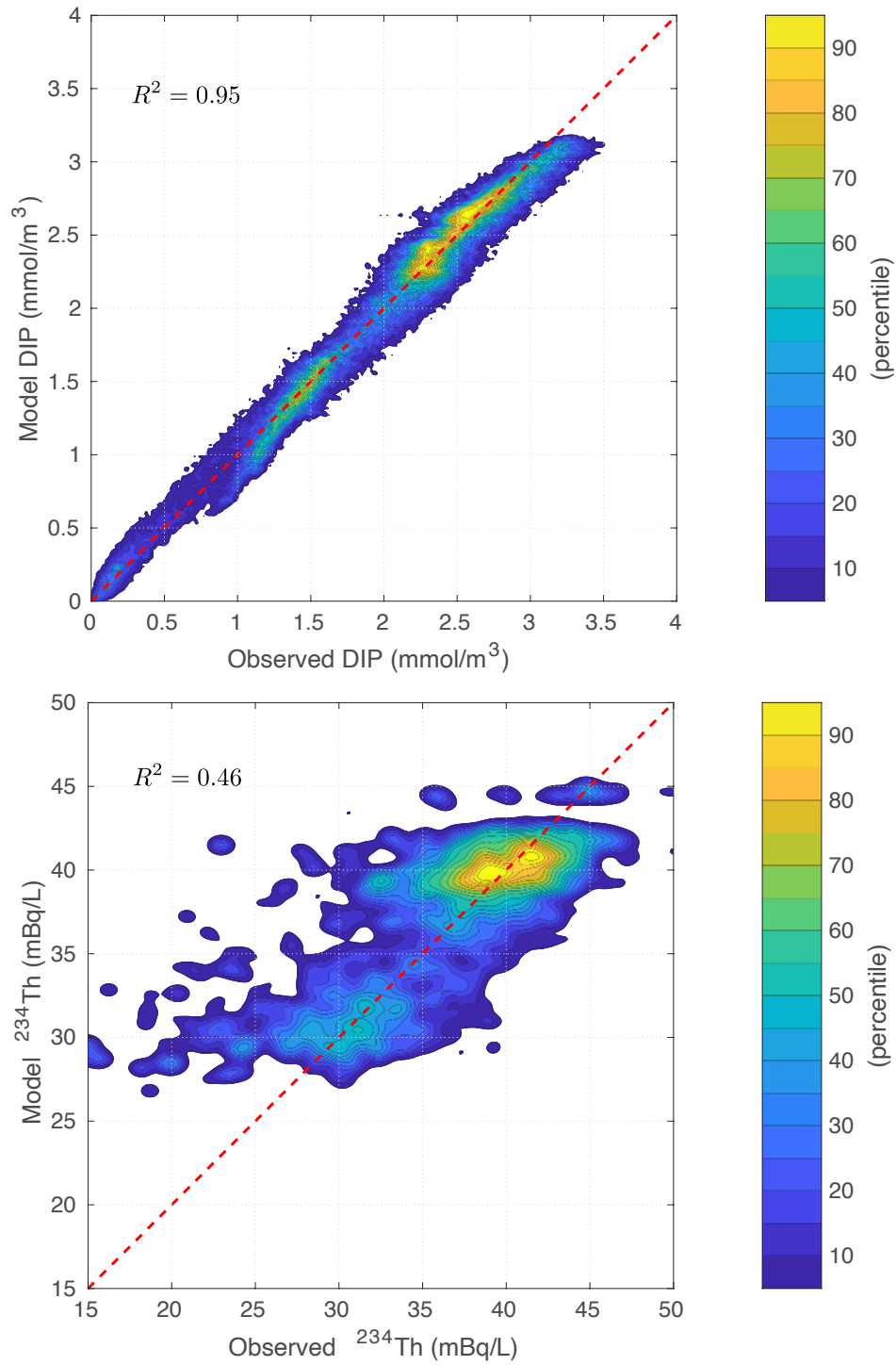


Figure A2. Comparison of model tracers with observed ones. 1) Model DIP versus WOA2013 climatology DIP concentration. 2) Model total ²³⁴Th (dissolved + particulate) versus observation.

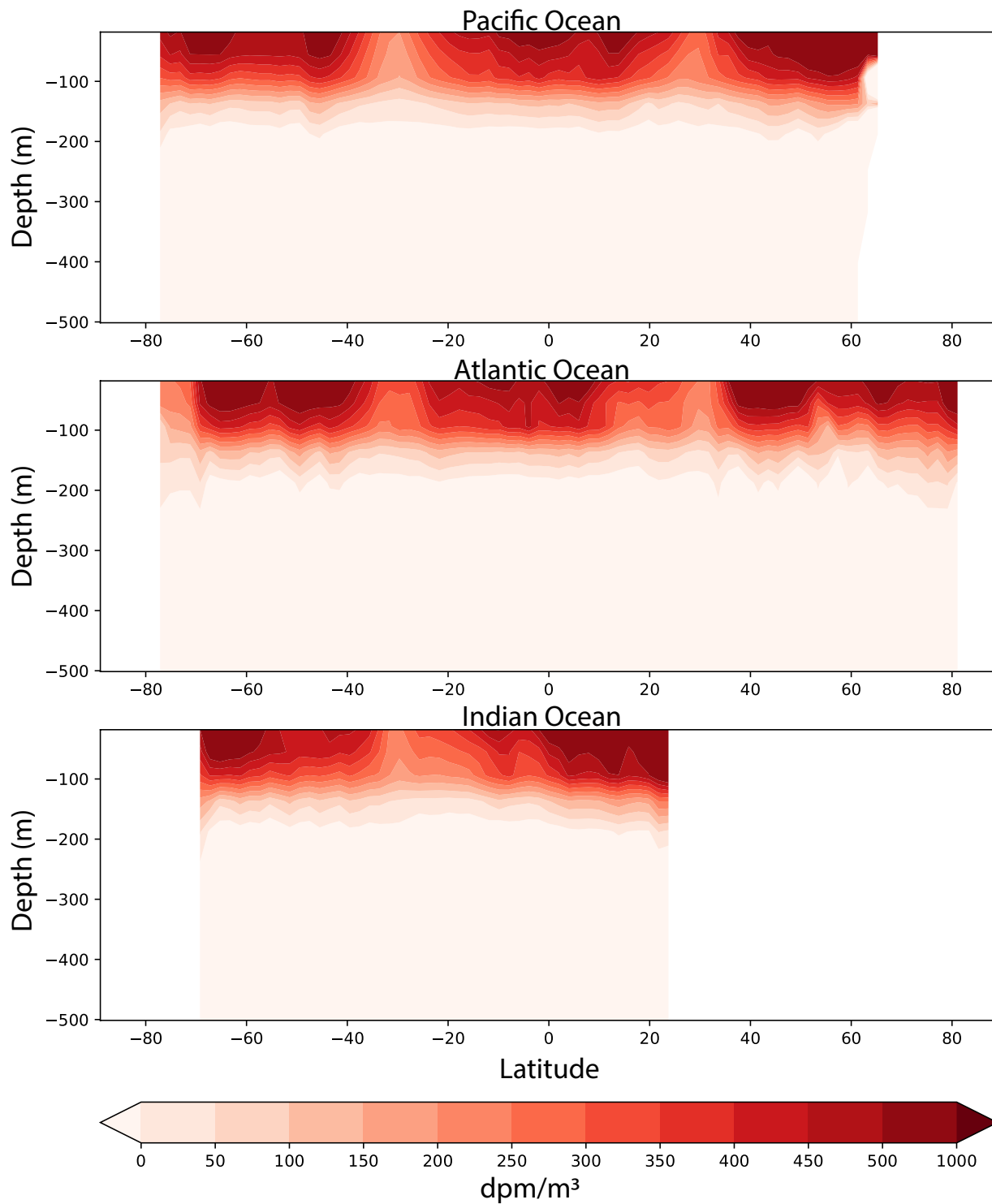


Figure A3. Zonal mean difference between ^{238}U and ^{234}Th for the three major basins.

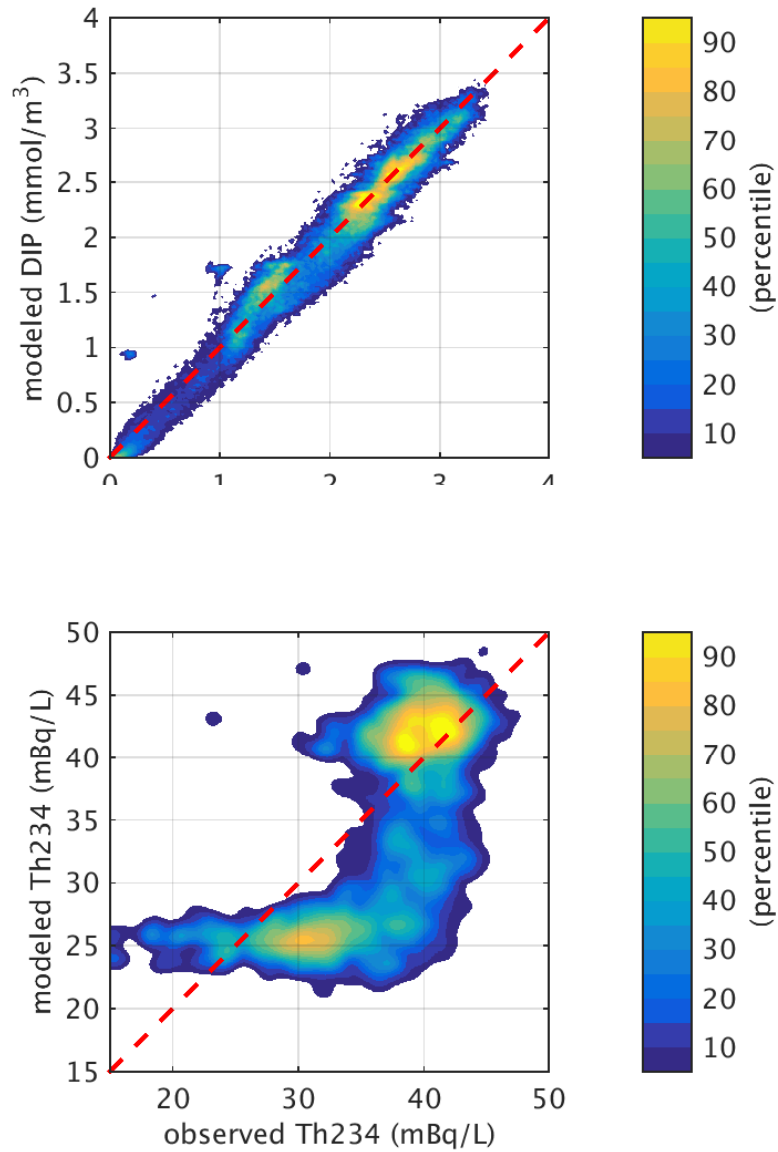


Figure A4. Comparison of observed and modeled tracers based on Galbraith and Martiny *Galbraith and Martiny* [2015] C:P parameterization. 1) Model DIP versus WOA2013 climatology DIP concentration. 2) Model total ²³⁴Th (dissolved + particulate) versus observation.